© 2022. Published by The Company of Biologists Ltd | Journal of Cell Science (2022) 135, jcs259743. doi:10.1242/jcs.259743

RESEARCH ARTICLE

Vps68 cooperates with ESCRT-III in intraluminal vesicle formation

Sören Alsleben and Ralf Kölling*

ABSTRACT

The endosomal sorting complex required for transport (ESCRT)-III mediates budding and abscission of intraluminal vesicles (ILVs) into multivesicular endosomes. To further define the role of the yeast ESCRT-III-associated protein Mos10 (also known as Vps60) in ILV formation, we screened for new interaction partners by using stable isotope labeling of amino acids in cell culture (SILAC) and mass spectrometry. Here, we focused on the newly identified interaction partner Vps68. Our data suggest that Vps68 cooperates with ESCRT-III in ILV formation. The deletion of *VPS68* caused a sorting defect similar to that of the *SNF7* deletion strain when the cargo load was high. The composition of ESCRT-III was altered, the level of core components was higher and the level of associated proteins was lower in the *VPS68* deletion strain. Our data further indicate that at some point in the functional cycle of ESCRT-III, Snf7 could be replaced by Mos10. Vps68 has an unusual membrane topology. Two of its potential membrane helices are amphipathic helices that localize to the luminal side of the endosomal membrane. Based on this membrane topology, we propose that Vps68 and ESCRT-III cooperate in the abscission step by weakening the luminal and cytosolic leaflets of the bilayer at the abscission site.

KEY WORDS: Endocytosis, Multivesicular body, Intraluminal vesicles

INTRODUCTION

Endosomal sorting complex required for transport (ESCRT)-III proteins are membrane remodeling factors that are involved in the deformation and abscission of membranes. ESCRT-III participates in a large number of membrane-related cellular processes (Gatta and Carlton, 2019; Hurley, 2015; McCullough et al., 2018; Vietri et al., 2020). Initially, ESCRT-III proteins were identified in yeast as factors involved in the formation of intraluminal vesicles (ILVs) at late endosomes (Babst et al., 2002); however, it is now clear that ESCRT-III proteins are an inherent part of all eukaryotic cells. ESCRT-III proteins are of ancient origin; they were already present in the last common eukaryotic ancestor (LCEA) (Leung et al., 2008). Recent reports indicate that the ESCRT-III function may be even more general and widespread than initially thought. Cryo-electron microscopy studies have shown that the bacterial phage shock protein PspA and the plant chloroplast protein Vipp1 share a common evolutionary origin with ESCRT-III proteins (Junglas et al., 2021; Liu et al., 2021). Most ESCRT-III proteins have the propensity to form filaments. The structure of the ESCRT-III assemblies has been meticulously studied *in vitro* (Banjade et al., 2019; Bertin et al., 2020; Chiaruttini et al., 2015; Lee et al., 2015; Maity et al., 2019; Tang et al., 2015), but how ESCRT-III looks *in vivo* is still unclear. If ESCRT-III forms structures similar to those of PspA and Vipp1, the complex may be less extensive than suggested by the previous *in vitro* studies.

In yeast, the role of ESCRT-III in the formation of ILVs has been thoroughly studied. It is thought that the recruitment of ESCRT-III to the endosomal membrane is the final step in a cascade of reactions involving the upstream complexes ESCRT-0, -I and -II (Teis et al., 2008). The common view is that ESCRT-III itself is assembled in a stepwise manner. First, Vps20 is recruited by binding to the ESCRT-II subunit Vps25, then Snf7 enters and is induced to polymerize. Snf7 polymerization is limited by Vps2 (also known as Did4) and Vps24, which finally initiate disassembly of the complex by the AAA-ATPase Vps4. This view has been challenged recently (Adell et al., 2017; Mierzwa et al., 2017). According to these newer findings, there seems to be a continuous, stochastic exchange of ESCRT-III proteins and Vps4 at sites of ILV formation. Thus, ESCRT-III appears to be far more dynamic than originally thought.

The ESCRT-III protein family consists of eight members in yeast and twelve members in mammalian cells. With respect to ILV formation, the ESCRT-III proteins are conventionally divided into two groups, the so-called core subunits Snf7, Vps2, Vps20 and Vps24 (ESCRT-III proper); and the ESCRT-III-associated proteins Did2, Ist1 and Mos10 (also known as Vps60) (Azmi et al., 2008; Dimaano et al., 2008; Rue et al., 2008). The eighth member of the family, Chm7, is not involved in ILV formation but rather plays a separated role at the nuclear membrane (Bauer et al., 2015; Thaller et al., 2019). Our recent data suggest that the distinction between core components and associated ESCRT-III proteins may not be justified (Heinzle et al., 2019). We think that Did2 and Mos10 are an integral part of ESCRT-III. This view is supported by another study that investigated the contribution of Did2 and Ist1 to ESCRT-III function (Pfitzner et al., 2020).

There are conflicting reports as to the role of the so-called ESCRT-III-associated proteins. In our initial identification and characterization of Mos10, the *MOS10* deletion mutant was found to have a sorting defect indistinguishable from that observed upon deletion of other ESCRT-III core subunits (Kranz et al., 2001). In another report, the *MOS10* deletion only showed a sorting effect in combination with deletions of other ESCRT-III-associated factors (Rue et al., 2008). Recently, at least a partial sorting defect of the *MOS10* deletion strain has been reported in several studies (Banjade et al., 2021; Nickerson et al., 2010).

The impact of ESCRT-III deletions on the morphology of multivesicular endosomes has been studied by electron tomography (Nickerson et al., 2010, 2006). From these studies, a clear distinction can be made between core subunits and associated proteins. Deletion of core subunits completely prevents ILV formation and leads to the accumulation of stacked membrane structures next to the vacuole (the so-called class E compartments) (Raymond et al., 1992). In contrast, deletion of associated factors

Institut für Lebensmittelwissenschaft und Biotechnologie, Fg. Hefegenetik und Gärungstechnologie, Universität Hohenheim, 70599 Stuttgart, Germany.

*Author for correspondence (ralf.koelling@uni-hohenheim.de)

R.K., 0000-0002-8024-5686

Handling Editor: David Stephens
Received 4 January 2022; Accepted 31 March 2022

Journal of Cell Science (2022) 135, jcs259743. doi:10.1242/jcs.259743

gives rise to multivesicular endosomes with a vesicular-tubular endosome (VTE) morphology (Nickerson et al., 2010). Thus, the associated factors seem to act after the core components. Evidence has been presented that the associated proteins Did2 and Mos10 are involved in the disassembly of ESCRT-III (Azmi et al., 2008; Dimaano et al., 2008; Rue et al., 2008). Our interpretation of these findings is that ESCRT-III can exist in different functional states with different compositions. At the beginning of the functional cycle ESCRT-III is actively involved in ILV formation and/or abscission, then after completion of ILV formation, it is converted to a disassembly-competent complex. The data presented in this report are in line with this interpretation.

To learn more about the function of Mos10, we looked for new interaction partners by a stable isotope labeling of amino acids in cell culture (SILAC)-based mass spectrometry screen. So far, only Vta1 has been firmly established as a Mos10 interaction partner (Azmi et al., 2006). In our study, the ESCRT-III proteins Vps2, Vps24, Snf7 and Did2 were consistently co-purified with Mos10. This strengthens the view that Mos10 is an integral part of ESCRT-III. In addition, several other potential candidates were detected. Here, we focused on one of these interaction partners, the protein Vps68. Vps68 was first identified in a screen for vacuolar protein sorting (*vps*) mutants that mislocalize carboxypeptidase Y (Bonangelino et al., 2002). By genome-wide screens, it has been shown that Vps68 localizes to endosomes and that it forms a complex with Vps55 (Huh et al., 2003; Schluter et al., 2008). Here, we show that Vps68 physically interacts with ESCRT-III and present evidence that it cooperates with ESCRT-III in ILV formation.

RESULTS

Screen for Mos10-interacting proteins

Although the ESCRT-III system has been intensively studied, there are only relatively few reports about the role of the human ESCRT-III protein CHMP5 or its yeast counterpart Mos10. To learn more about the function of Mos10, we looked for novel Mos10 interaction partners. To this end, Mos10 was purified from yeast cell extracts by affinity chromatography, and the co-purified proteins were then identified by mass spectrometry. Purifications were performed with two different tags fused to the Mos10 C terminus, a 6×His tag (6His) and a superfolder GFP (sfGFP) tag. Mos10–6His was functional (Fig. S4), whereas Mos10–sfGFP gave rise to a block in endocytic trafficking (Fig. S5). To filter out unspecific binding, a SILAC-based approach was used. The culture expressing tagged Mos10 was grown in medium containing arginine and lysine labeled with heavy isotopes, while the control culture expressing native Mos10 was grown with arginine and lysine with normal, light isotopes. Among the proteins identified by mass spectrometry, we looked for proteins with a high heavy to light (H/L) isotope abundance ratio, indicating specific interaction with the tagged form of Mos10. The results of three different purifications (two Ni-NTA purifications with the 6His tag, one with anti-GFP antibodies and the sfGFP tag) are summarized in Table S1. We detected 51 proteins that were at least 2-fold enriched for the heavy isotopes. Two of these proteins (Bag7 and Ykr075c) are naturally occurring poly-histidine proteins and are thus most likely unspecific contaminants. The list of potential interaction partners was checked against the CRAPome database (Mellacheruvu et al., 2013) to filter out common contaminants in affinity purification mass spectrometry experiments. Proteins detected at least five times in 17 experiments of the CRAPome database were dismissed as unspecific. The remaining 37 proteins were considered candidates for further study. The proteins with the highest H/L ratio, which were consistently co-purified in all three experiments, were the ESCRT-III proteins Vps2, Snf7, Vps24 and Did2. This clearly demonstrates that Mos10 is a bona fide member of ESCRT-III. From the list of the remaining proteins, Vps68 was selected for further study.

Vps68 binds to ESCRT-III

The binding of Vps68 to Mos10 was verified by a co-immunoprecipitation (co-IP) experiment. For detection, Vps68 was tagged with sfGFP at its N terminus. N-terminally tagged Vps68 proved to be functional, whereas C-terminally tagged Vps68 was compromised in its function (Fig. S2). Vps68 was immunoprecipitated from cell extracts using anti-GFP antibodies and examined for co-IP of the ESCRT-III proteins Mos10, Snf7 and Vps2 (Fig. 1A). In the otherwise wild-type background, all three ESCRT-III proteins could be co-immunoprecipitated by the GFP antibodies. This confirms our mass spectrometry identification of Vps68 as an interaction partner of Mos10.

We were then interested to know whether Vps68 is recruited to ESCRT-III by direct binding to Mos10 or whether the interaction is mediated by some other subunit of ESCRT-III. To this end, the co-IP experiment was repeated with a Δ*mos10* and a Δ*snf7* strain carrying the integrated *sfGFP–VPS68* cassette. As can be seen in Fig. 1A, Snf7 and Vps2 could still be precipitated by Vps68 in the Δ*mos10* strain. Thus, binding of Vps68 to ESCRT-III does not appear to be mediated by Mos10. In the Δ*snf7* strain, no co-precipitation of the examined ESCRT-III subunits could be observed. This is in line with the observation that Snf7 is absolutely essential for ESCRT-III formation (Heinzle et al., 2019) and indicates that in the Δ*snf7* strain there is no ESCRT-III that can be precipitated by Vps68. Thus, we cannot say through which subunit Vps68 interacts with ESCRT-III. The amount of Snf7 and Vps2 precipitated by Vps68 was 2–3 times higher in the Δ*mos10* strain compared to the amount precipitated in the wild-type strain (Fig. 1B). Thus, ESCRT-III complexes accumulate in the cell when Mos10 is missing. This is consistent with a role of Mos10 in disassembly of ESCRT-III.

This notion was explored further using sucrose density gradient fractionation of cell extracts from the wild-type strain and from a Δ*mos10* strain (Fig. 1C–E; Fig. S1). The fractionation profile of Snf7 was compared to the profiles of two marker proteins: Pep12 as a marker for endosomes and ALP (alkaline phosphatase, also known as Pho8) as a marker for the vacuole. With wild-type extracts, Pep12 had a peak in fraction 7 and ALP had a peak in fraction 9. In the Δ*mos10* strain, the Pep12 peak was shifted towards fraction 8, whereas the ALP peak was unchanged. With wild-type extracts, most of the Snf7 was found at the top of the gradient, where soluble proteins are localized. A small proportion of the Snf7 migrated into the gradient and formed a small peak in fraction 7, consistent with an endosomal localization of Snf7. With Δ*mos10* extracts, the membrane-associated fraction of Snf7 was markedly higher in abundance, with a concomitant reduction in abundance of the soluble fraction. The peak was shifted to fraction 8, matching the Pep12 peak. This agrees with our co-IP results and shows that Mos10 is involved in the disassembly of ESCRT-III.

Vps68 is involved in the sorting of the endocytic cargo protein Ste6

Vps68 has been identified previously as a protein involved in the trafficking of proteins to the yeast vacuole (Bonangelino et al., 2002; Huh et al., 2003; Schluter et al., 2008). To further explore its role in endocytic trafficking and to gain information about how Vps68 intersects with ESCRT-III function, the effect of *VPS68* deletion on

Journal of Cell Science (2022) 135, jcs259743. doi:10.1242/jcs.259743

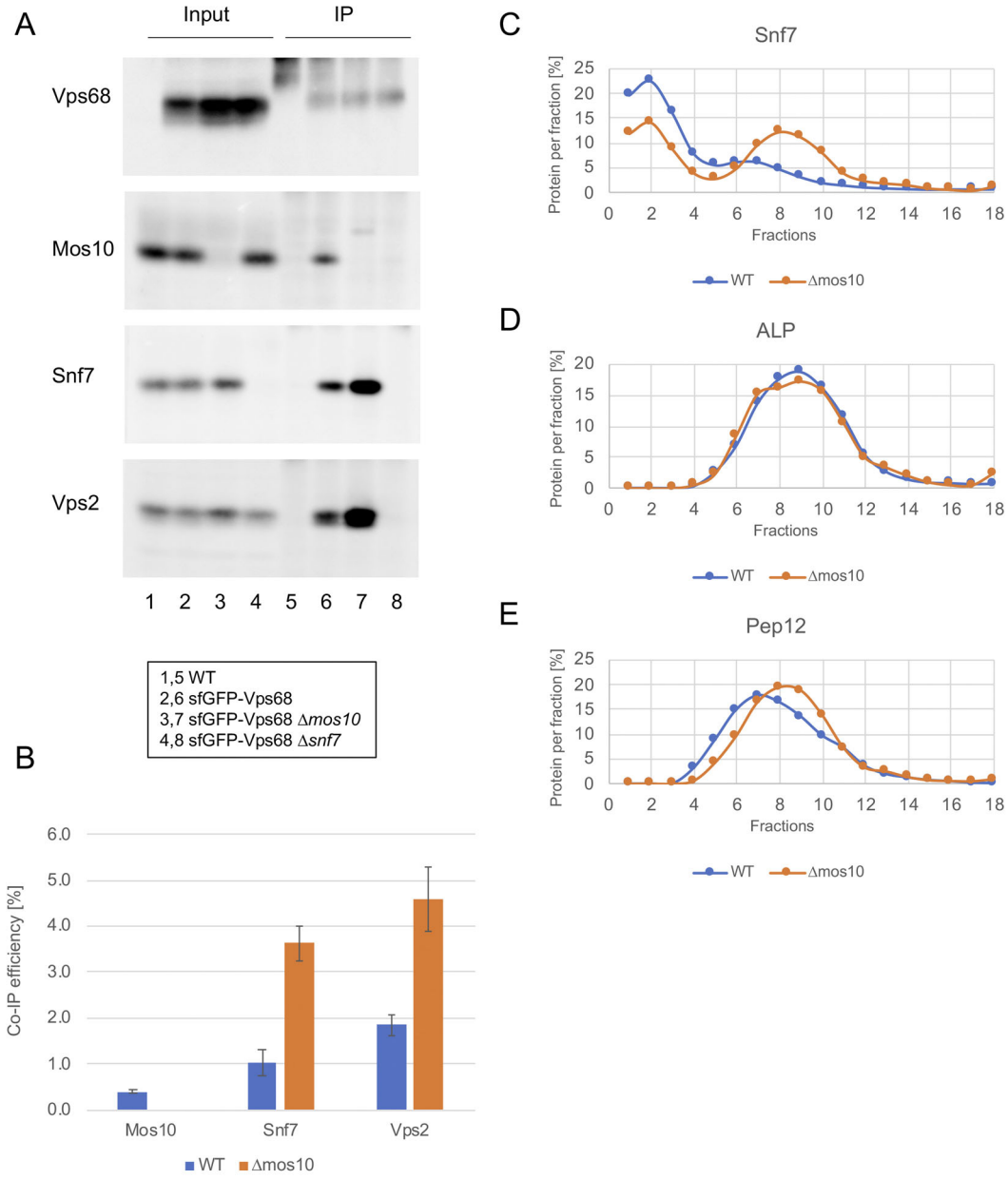

Fig. 1. Vps68 binds to ESCRT-III. (A) sfGFP–Vps68 was immunoprecipitated from cell extracts using anti-GFP antibodies. The immunoprecipitates (IPs) were examined for the presence of ESCRT-III proteins using the indicated specific antibodies. Lanes 1–4, input (2% of the lysate for co-IP; 50% of the lysate for Vps68 IP).; lanes 5–8: IPs. Lanes 1 and 5: RKY1558 (wild-type strain, WT); lanes 2 and 6: RKY3285 (*sfGFP–VPS68*); lanes 3 and 7: RKY3394 (*sfGFP–VPS68 Δmos10*); lanes 4 and 8: RKY3412 (*sfGFP–VPS68 Δsnf7*). (B) Quantification of the co-IP efficiencies (mean±s.d. of three independent experiments). Blue columns, RKY3285 (*sfGFP–VPS68*, WT); orange columns, RKY3394 (*sfGFP–VPS68 Δmos10*, *Δmos10*). (C–E) Membrane accumulation of Snf7 in a *MOS10* deletion mutant. Yeast cell extracts of the wild-type strain RKY1558 (WT, blue) and the *Δmos10* strain RKY2909 (orange) were fractionated by sucrose density gradient fractionation and analyzed by western blotting. (C) Snf7, (D) alkaline phosphatase (ALP), (E) Pep12. The western blot signals (Fig. S1) were quantified using ImageJ. The percentage of total protein per fraction is shown on the *y*-axis. Fraction numbers on the *x*-axis range from low density (1) to high density (18). Data are the average of two independent experiments.

the endocytic cargo protein Ste6 was examined. The ATP-binding cassette (ABC) transporter Ste6 is a very short-lived protein (Kölling and Hollenberg, 1994). After transport to the plasma membrane, it is internalized by endocytosis and moves to the vacuole for degradation. To see whether Vps68 is required for Ste6 transport to the vacuole, the half-life of Ste6 was determined by a Gal-depletion experiment in a wild-type strain and in a *VPS68* deletion strain (Fig. 2). Ste6 was expressed from a *GAL1* promoter inserted in front of the chromosomal *STE6* gene. Cells were grown in medium containing galactose to induce expression from the *GAL1* promoter and were then shifted to glucose-containing medium to repress transcription. In the wild-type strain, Ste6 was degraded with a half-life of 13 min. In the *Δvps68* strain, there was a slight delay in the degradation of Ste6 after the shift to glucose-containing medium, and then Ste6 was degraded with a half-life of 23 min. Thus, Ste6 is moderately stabilized in the *VPS68* deletion strain. Similar results have been reported for the a-factor receptor Ste3 (Schluter et al., 2008).

To determine the site of action of Vps68 in the endocytic pathway, an epistasis analysis with established markers was

Journal of Cell Science (2022) 135, jcs259743. doi:10.1242/jcs.259743

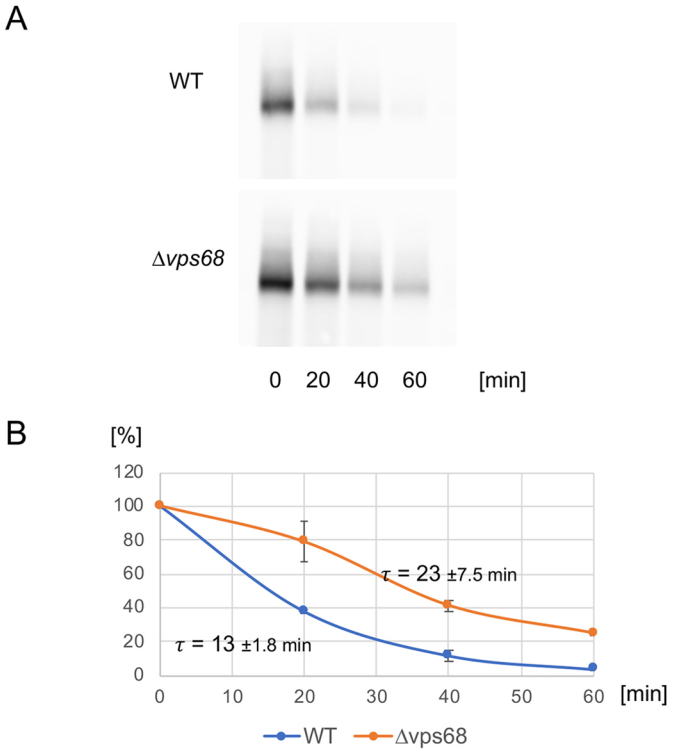

Fig. 2. *VPS68* deletion stabilizes Ste6, as assayed in a Gal-depletion experiment. (A) Yeast cells were grown on 2% galactose medium and shifted to 2% glucose medium at t_0. Cell extracts from equal culture volumes were prepared at the times indicated and examined for Ste6 by western blotting. Strains: wild type (WT), RKY3319; Δ*vps68*, RKY3320. (B) The western blot signals as described for A were quantified using ImageJ (band intensity at t_0=100%). Ste6 half-lives are indicated (mean±s.d.). Data are presented as mean±s.d. of two independent experiments.

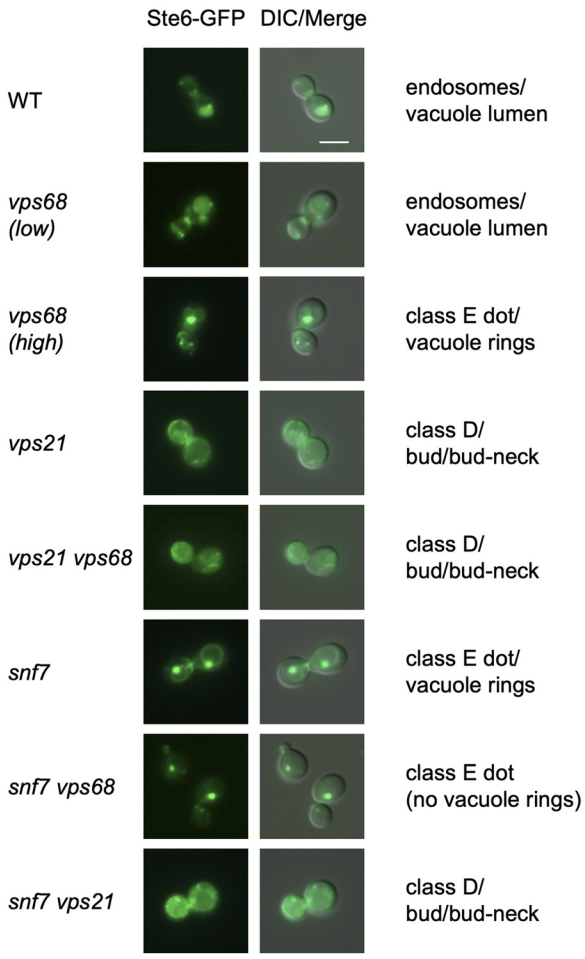

Fig. 3. Influence of *VPS68* deletion on Ste6–GFP localization. Different yeast strains were transformed with the Ste6–GFP plasmid pRK599. The localization of Ste6–GFP was examined by fluorescence microscopy. Strains (from top to bottom): RKY1558 (wild type, WT), RKY3222 (Δ*vps68*, low expression level of Ste6–GFP), RKY3222 (Δ*vps68*, high expression level of Ste6–GFP), RKY1920 (Δ*vps21*), RKY3307 (Δ*vps21* Δ*vps68*), RKY2790 (Δ*snf7*), RKY3300 (Δ*snf7* Δ*vps68*), RKY3376 (Δ*snf7* Δ*vps21*). Left panels, Ste6–GFP fluorescence; right panels, merged picture of differential interference contrast (DIC) image and fluorescence image. The observed Ste6 labeling pattern in the different strains is indicated on the right side of the figure. Images are representative of at least 100 cells. Scale bar (top right panel): 5 µm.

performed. The localization of Ste6–GFP expressed from a multicopy plasmid in different single and double mutant strains was examined by fluorescence microscopy (Fig. 3). In the wild-type strain, Ste6–GFP labeled the lumen of the vacuole and occasionally some endosomal dots. In the class D mutant Δ*vps21*, which has a defect in the fusion of endocytic vesicles with the endosome (Bowers and Stevens, 2005), Ste6–GFP displays enhanced recycling to the yeast cell surface (Krsmanović et al., 2005). In this mutant, we observed Ste6–GFP fluorescence at a number of smaller vesicles concentrated at the bud neck and some localization to the bud surface. No labeling of the vacuolar lumen was visible. The Δ*snf7* mutant displayed the classical class E phenotype, with a large patch of Ste6–GFP fluorescence at the vacuole, as well as labeling of the vacuolar membrane (Raymond et al., 1992). Curiously, the phenotype of the *VPS68* deletion was dependent on the expression level of Ste6–GFP. The copy number of the 2µ vector used for expression of Ste6–GFP varies considerably, thus some cells had a very high expression level and other cells expressed Ste6–GFP only at low levels. With low-level expression, the pattern of Ste6–GFP fluorescence in Δ*vps68* cells resembled that in wild-type cells, with a somewhat more pronounced labeling of endosomal dots. In contrast, Δ*vps68* cells with high Ste6–GFP expression levels showed a brightly labeled patch at the vacuole with a faint labeling of the vacuolar membrane, similar to a class E phenotype.

For the epistasis analysis, Ste6–GFP fluorescence was examined in double mutants. The Δ*vps21* Δ*vps68* double mutant clearly looked like the Δ*vps21* single mutant, thus Δ*vps21* is epistatic over the Δ*vps68* mutant, indicating that Vps21 acts before Vps68. A similar result was obtained for the Δ*snf7* Δ*vps21* double mutant, which resembled the Δ*vps21* single mutant. When Δ*snf7* and Δ*vps68* were combined, a class E-like phenotype was observed with the notable difference that the labeling of the vacuolar membrane was missing. This synthetic phenotype indicates that Vps68 and Snf7 act at the same step.

We also examined the localization of sfGFP–Vps68 (Fig. S4B). In agreement with a previous report (Schluter et al., 2008), we detected a handful of distinct dots, which presumably correspond to endosomes. In a Δ*snf7* background, Vps68 was trapped in class E structures. Thus, it is very likely that Vps68 acts at the level of the endosome, as reported previously.

The *VPS68* deletion alters ESCRT-III composition

To further explore the relationship between Vps68 and ESCRT-III, we looked for differences in the composition of ESCRT-III in Δ*vps68* cells compared to that in wild-type cells. ESCRT-III was

Journal of Cell Science (2022) 135, jcs259743. doi:10.1242/jcs.259743

immunoprecipitated from cell extracts with antibodies against Did2, Ist1, Mos10, Snf7, Vps2 and Vps24 (Chm7 was omitted because it is not part of the endosomal complex, and Vps20 was omitted due to low signal intensity). The immunoprecipitates were then analyzed for co-IP of the other ESCRT-III proteins. The co-IP signals were quantified, and the wild-type co-IP efficiencies were subtracted from the co-IP efficiencies of the Δ*vps68* strain (Fig. 4; blots in Fig. S3). As can be seen in Fig. 4, a striking division among the different ESCRT-III proteins was observed. While the complexes precipitated from Δ*vps68* cells contained less Did2, Ist1 and Mos10 compared to those precipitated from wild-type cells, they contained more Snf7, Vps2 and Vps24. Snf7, Vps2 and Vps24 are the core ESCRT-III components, which are thought to be actively involved in ILV formation and abscission. Did2, Ist1 and Mos10 are the ESCRT-III-associated proteins, which are thought to be involved in disassembly of ESCRT-III (Azmi et al., 2008; Dimaano et al., 2008; Rue et al., 2008). Our results suggest that *VPS68* deletion interferes with the transition from an ILV-forming ESCRT-III complex to a disassembly-competent complex.

Effect of *VPS68* deletion on the localization of ESCRT-III proteins

Vps68 could act as a scaffold or adapter for ESCRT-III membrane association. Therefore, we examined the effect of the *VPS68* deletion on membrane association of ESCRT-III proteins by a flotation experiment (data not shown). Only minor differences in the membrane-associated fractions between Δ*vps68* and wild-type strains were observed. In general, ∼30–50% of the ESCRT-III proteins were found to be membrane associated. The only exception was Mos10, which had a very low level of membrane association of ∼10%. This experiment shows that Vps68 is not required for membrane association of ESCRT-III; however, it could affect the site of membrane association of ESCRT-III proteins within the cell.

To examine the intracellular localization in the *VPS68* deletion strain versus wild type, all ESCRT-III proteins were C-terminally tagged with sfGFP by the insertion of a tagging cassette into the yeast genome. Since it is known that tagging of ESCRT-III proteins can lead to non-functional proteins, we tested the functionality of the tagged proteins. The strains were transformed with a single-copy plasmid expressing an mCherry-tagged variant of the vacuolar carboxypeptidase S (Cps1). Cps1 is transported to the lumen of the vacuole via the multivesicular body (MVB) pathway. The localization of mCherry–Cps1 was examined using fluorescence microscopy (Figs S4 and S5). In the wild-type strain, mCherry–Cps1 exclusively labeled the lumen of the vacuole. In the Δ*vps24* mutant – used as a reference – a typical class E localization was observed. The strain expressing Mos10–6His displayed a wild-type pattern, showing that the tagged protein is functional. The ESCRT-III–sfGFP fusions were compromised in their function to different degrees. While the mCherry-Cps1 labeling in the *IST1–sfGFP* strain was indistinguishable from that observed in the wild-type strain, the *SNF7–*, *VPS2–* and *VPS24–sfGFP* strains gave rise to a strong class E phenotype. The *DID2–* and *MOS10–sfGFP* strains showed a partial defect, with some luminal fluorescence, but also a clearly visible vacuolar rim labeling. Although most of the tagged ESCRT-III proteins cannot support normal transport of endocytic cargo proteins to the lumen of the vacuole, they may still be useful for localization studies, because, as described below, the observed fluorescence patterns are compatible with endocytic compartments.

The ESCRT-III proteins could be broadly divided into two groups with respect to localization patterns of their sfGFP fusions (Fig. 5). Did2 and Ist1 looked very similar, with about half a dozen distinct fluorescent puncta. With Snf7 and Vps2, a brightly labeled cluster of vesicles and a number of less intensively labeled vesicles, which tended to be concentrated at the cell cortex,

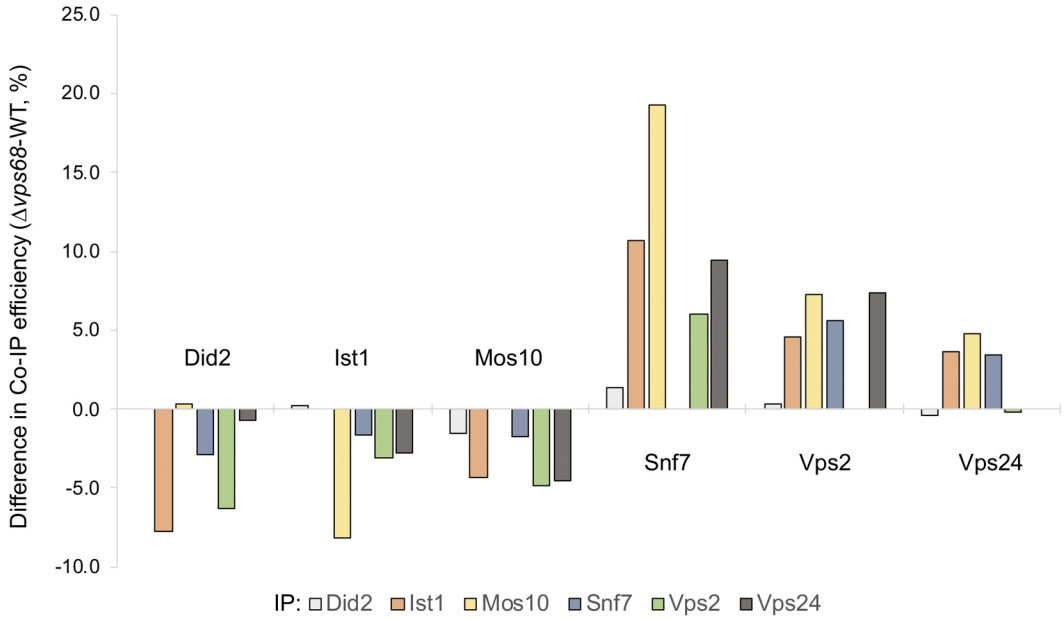

Fig. 4. Altered ESCRT-III composition in Δ*vps68* cells. Did2, Ist1, Mos10, Snf7, Vps2 and Vps24 were immunoprecipitated from cell extracts of RKY1558 (wild type, WT) and RKY3222 (Δ*vps68*) strains. The immunoprecipitates were examined for co-IP of other ESCRT-III proteins by western blotting. The co-IP signals (Fig. S3) were quantified using ImageJ. The percentage of protein that could be co-immunoprecipitated was calculated (co-IP efficiency). Co-IP efficiencies were normalized to the primary immunoprecipitation (IP) efficiency of the bait protein. The co-IP efficiencies of the wild-type strain were subtracted from the co-IP efficiencies of the Δ*vps68* strain. The co-immunoprecipitated proteins are indicated above or below the columns. The color code for the proteins precipitated in the primary IP is shown beneath the graph. Data are the average of two independent experiments.

Journal of Cell Science (2022) 135, jcs259743. doi:10.1242/jcs.259743

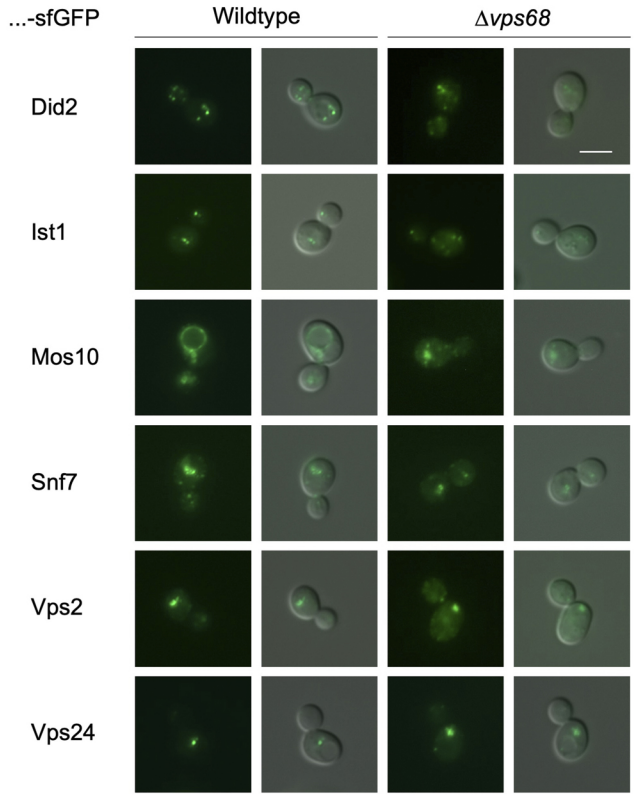

Fig. 5. Intracellular localization of ESCRT-III–sfGFP fusions. The intracellular localization of ESCRT-III–sfGFP fusions expressed from their chromosomal loci was examined using fluorescence microscopy. Left panels, wild-type background; right panels, Δ*vps68* background. For each set, GFP fluorescence (left) and a merged image (GFP fluorescence and differential interference contrast; right) are shown. Strains, from top to bottom (wild type and Δ*vps68* background, respectively): Did2–sfGFP, RKY3214 and RKY3269; Ist1–sfGFP, RKY3215 and RKY3257; Mos10–sfGFP, RKY3216 and RKY3224; Snf7–sfGFP, RKY3217 and RKY3279; Vps2–sfGFP, RKY3218 and RKY3271; Vps24–sfGFP, RKY3220 and RKY3274. Images are representative of at least 100 cells. Scale bar (top right panel): 5 µm

were observed. Vps24 resembled Snf7 and Vps2 in the sense that it also showed a brightly labeled cluster of vesicles, but in contrast to these proteins, it had fewer additional labeled vesicles. These localization patterns were not affected by *VPS68* deletion. Mos10–sfGFP, in contrast, showed a unique localization pattern. The labeling was concentrated around the vacuole in a patchy manner. This pattern is distinct from a class E phenotype, since the Mos10 patches were more numerous and not so grossly enlarged. This vacuolar Mos10–sfGFP labeling was completely lost in Δ*vps68* cells. In this mutant, the Mos10–sfGFP pattern resembled that of Snf7–sfGFP.

To further define the dot-like structures seen with the tagged ESCRT-III proteins, we compared the localization of Snf7–mCherry with the localization of sfGFP-tagged yeast Rab proteins, which serve as markers for different organelles (Fig. S6). The N-terminally tagged Rab proteins were expressed from the *SNF7* promoter at their chromosomal loci. As might have been expected, Snf7–mCherry colocalized with the Rab5 homolog Vps21, a thoroughly studied endosomal marker in yeast. The brightly labeled vesicular clusters were positive for both proteins. But the localization of the two proteins did not completely overlap, there were also vesicular structures that were only labeled by one or the other protein (marked by arrowheads in Fig. S6). Localization of the Rab5 homolog Ypt53 closely resembled that of Vps21. The third Rab5 homolog, Ypt52, showed an unusual labeling pattern; part of it also localized to the Snf7 clusters, but in addition, it stained endoplasmic reticulum (ER) membranes. Thus, Ypt52 could be involved in the transport of proteins between endosomes and the ER. This intriguing finding clearly deserves further study. Other Rab proteins, including proteins that are associated with the Golgi or post-Golgi compartments as part of the secretory pathway (Ypt6, Ypt31 and Ypt32), showed no colocalization with Snf7–mCherry. An interaction was observed between Snf7–mCherry and sfGFP–Ypt10. This protein is also considered as a Rab5 homolog and could play a role in endosome fusion to the vacuole (Langemeyer et al., 2020); however, so far not much is known about its function. When Ypt10 was tagged alone, labeling of the vacuolar membrane with a few associated dots was observed, reminiscent of the Mos10–sfGFP localization. However, this labeling was lost when Snf7–mCherry was present in the same strain. Apparently, Ypt10 association with endosomal and vacuolar structures requires successful completion of the ESCRT-III function, which is prevented by tagging Snf7 with mCherry.

Mos10 accumulates in endosomal structures at the vacuole

Mos10–sfGFP shows a unique circular localization around the vacuole. Imaging of *z*-stacks revealed that this labeling consists of vesicular and tubular structures that form an irregular network around the vacuole (data not shown). These structures could result from a proliferation of the vacuolar membrane, similar to the situation observed for Chm7, where an accumulation of the protein inside the nucleus leads to a dramatic proliferation of the inner nuclear membrane (Thaller et al., 2019). Alternatively, these structures could be derived from some other cellular compartment. To distinguish between these alternatives, the localization of Mos10 was compared with the localization of marker proteins by fluorescence microscopy. In some combinations, Mos10 was tagged with mCherry, in others it was tagged with sfGFP (Fig. 6). The switch of the tag was necessary because some of the marker proteins could not be visualized using an mCherry tag due to low fluorescence intensity. First, Mos10–sfGFP was compared with the vacuolar marker protein Vph1–mCherry. In contrast to Mos10, which displayed the usual irregular patchy localization, Vph1 showed a smooth, regular labeling of the vacuolar membrane. The vacuoles were evenly labeled, and no concentration in patches could be seen. From this we conclude that the Mos10–sfGFP structures are not derived from the vacuolar membrane, but are instead closely associated with it. These structures do not seem to be derived from ER or Golgi membranes, since no colocalization with the marker proteins Sec63 or Cog5 could be observed. With sfGFP–Vps21, a handful of distinct dots were observed, which were not labeled by Mos10–mCherry. In some cases, sfGFP–Vps21 dots were seen at the vacuolar membrane, but they did not coincide with Mos10–mCherry patches. Thus, it appears that Vps21 does not colocalize with the Mos10 structures. Next, we examined two cargo proteins of the endocytic pathway, Cps1 and Ste6, which are sorted to the vacuolar lumen via the MVB pathway. These two proteins labeled the vacuolar membrane and colocalized with Mos10 patches. From this we conclude that the Mos10–sfGFP structures at the vacuolar membrane are late endosomes.

Switch from a Snf7 complex to a Mos10 complex?

In a previous report, we examined the influence of ESCRT-III deletion mutations on the composition of ESCRT-III (Heinzle et al.,

Journal of Cell Science (2022) 135, jcs259743. doi:10.1242/jcs.259743

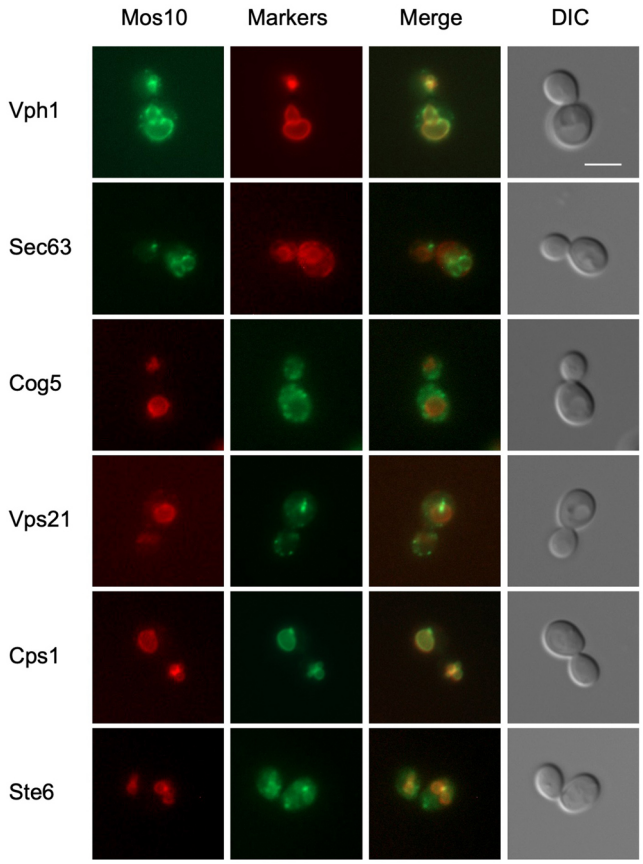

Fig. 6. Mos10 colocalizes with endosomal cargo proteins. Yeast strains expressing a chromosomal copy of tagged versions of Mos10 and the indicated specific marker proteins were examined for colocalization using fluorescence microscopy. The proteins were either tagged with sfGFP (green) or mCherry (red) depending on the signal intensity of the fusion proteins involved. Panels from left to right: Mos10 fluorescence (either sfGFP or mCherry), marker protein fluorescence (either mCherry or sfGfP), merged Mos10 and marker fluorescence image, differential interference contrast image. Strains from top to bottom: RKY3448 (Mos10–sfGFP, Vph1–mCherry), RKY3429 (Mos10–sfGFP, Sec63–mCherry), RKY3482 (Mos10–mCherry, Cog5–sfGFP), RKY3473 (Mos10–mCherry, sfGFP–Vps21), RKY3484 (Mos10–mCherry, Cps1–sfGFP) and RKY3486 (Mos10–mCherry, Ste6–sfGFP). Images are representative of at least 100 cells. Scale bar (top right panel): 5 µm.

2019). We made the observation that anti-Mos10 antibodies co-immunoprecipitated most of the other ESCRT-III proteins but not Snf7. This opened up the possibility that at a certain point in the ESCRT-III functional cycle Snf7 is replaced by Mos10, which could convert the active ESCRT-III complex into a disassembly-competent complex. However, there was a caveat to this experiment. The anti-Mos10 antibodies showed a small degree of cross-reactivity towards Snf7, so we had to introduce a correction factor for this cross-reactivity. The correction factor was obtained from the anti-Mos10 immunoprecipitation in a Δ*mos10* background. Any Snf7 signal obtained under these conditions must be derived from the direct immunoprecipitation of Snf7. This value was subtracted from the Snf7 co-IP signals in anti-Mos10 immunoprecipitations. With this correction, no Snf7 co-IP was obtained with anti-Mos10 antibody; however, there is the possibility that we overcorrected. The direct immunoprecipitation of Snf7 by the anti-Mos10 antibody could be lower or even non-existent in the presence of Mos10 protein.

To exclude this potential problem, we performed a pulldown experiment with Mos10–6His, which was purified from cell extracts using Ni-NTA. The proteins purified on the Ni-NTA beads were tested for the presence of ESCRT-III proteins by western blotting with specific antibodies. As can be seen in Fig. 7, substantial amounts of Vps2 and Vps24 were co-purified with Mos10–6His. The Snf7 signal, however, was extremely low and close to the background signal obtained with the negative control strain. Thus, Snf7 is at the most only present in very low amounts in the Mos10 complex. This is in line with our previous findings and shows that the performed correction was appropriate. The co-IP efficiency for Vps2 was 3-fold higher that for Vps24. This indicates that Vps2 could be a direct binding partner of Mos10.

We wondered whether the complex purified with Mos10–6His corresponded to the well-known endosomal complex involved in ILV formation or whether we purified a novel previously uncharacterized complex. To this end, we also performed a pulldown experiment in a Δ*snf7* background. Strikingly, no co-purification of Vps2 and Vps24 could be observed under these conditions. This demonstrates that although Mos10–6His brings down barely any Snf7 or no Snf7 at all, the purified complex is nevertheless completely dependent on Snf7. To reconcile these findings, we propose that Snf7 initiates ESCRT-III formation and that after completion of the ESCRT-III function it is replaced by Mos10, which then triggers disassembly of the complex.

This notion is supported by fluorescence microscopy of Mos10–sfGFP structures. We could show that the localization of Mos10–sfGFP to endosomal structures at the vacuole is completely dependent on the ‘upstream’ ESCRT-III proteins Vps20, Snf7, Vps2 and Vps24 (data not shown). In the respective deletion mutants, Mos10–sfGFP was completely cytosolic. By double-labeling experiments, we could further show that the Mos10–sfGFP patches at the vacuole also contain Vps2 and Vps24 (Fig. S7). This is in line with the Ni-NTA pulldown experiments. In the Mos10–sfGFP Snf7–mCherry strain, the Mos10 signal at the vacuole was lost. Instead, Mos10–sfGFP now localized to the bright Snf7–mCherry clusters and to smaller vesicles. Thus, Snf7–mCherry tagging leads to the same phenotype as *VPS68* deletion. This indicates that Snf7 and Vps68 act together at the same step. Also of note, the phenotype of Snf7 tagging was different from the phenotype of the *SNF7* deletion. This shows that Snf7–mCherry is not a completely non-functional protein, but that it preserves part of the Snf7 function.

Membrane topology of Vps68

Vps68 is a membrane protein with four predicted transmembrane helices (TMs). At least one of the four helices (helix 2) appears to be an amphipathic helix (AH) with an asymmetric distribution of hydrophilic and hydrophobic amino acids and a high hydrophobic moment ($<\mu_H>$) (Fig. S8A). Vps68 resembles Nce102 in its structure. Nce102 is localized to plasma membrane invaginations called eisosomes. It has an unusual membrane topology with four potential TMs, where only TM1 and TM4 span the membrane, while TM2 and TM3 are localized to the external space (Loibl et al., 2010). To see whether Vps68 has a similar topology, a membrane topology analysis similar to the one described for Nce102 was performed.

To probe the topology of Vps68, different N-terminal fragments of Vps68 were fused to the first 307 amino acids of mature invertase (Suc2) followed by a version of His4 with the first 33 amino acids deleted (His4C) (Sengstag et al., 1990). Three HA tags were inserted between the Vps68 and the Suc2 portions for western blot

Journal of Cell Science (2022) 135, jcs259743. doi:10.1242/jcs.259743

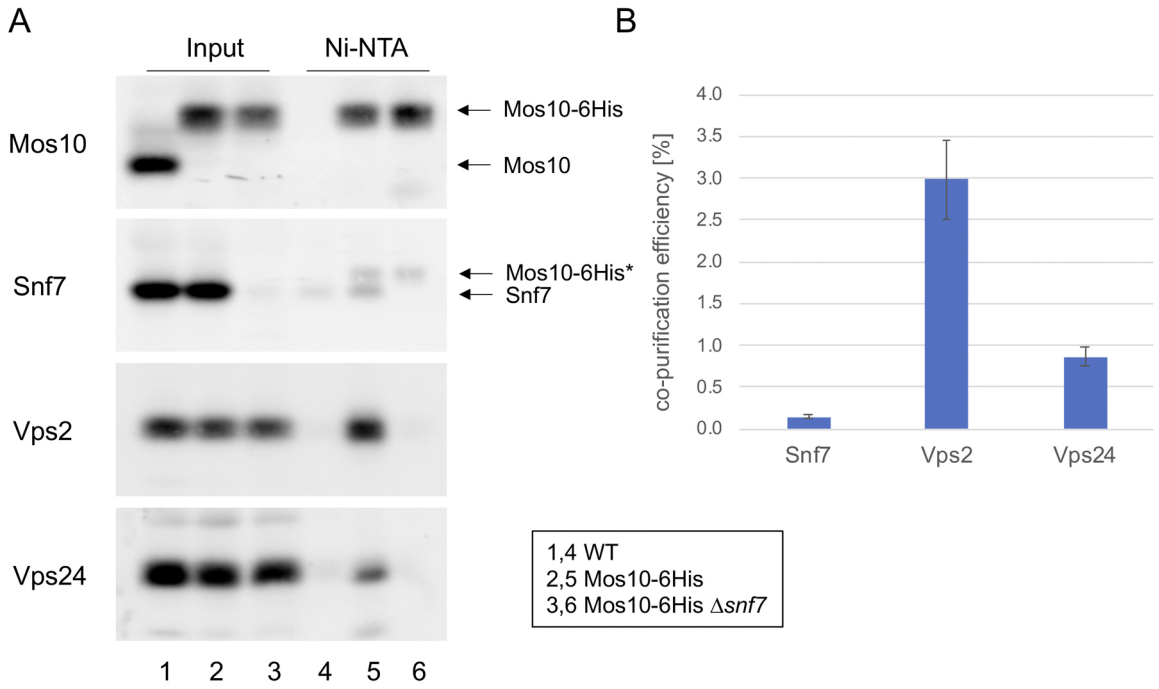

Fig. 7. Mos10–6His pulldowns. (A) Mos10–6His was purified from cell extracts by Ni-NTA affinity chromatography. The purified proteins were examined for co-purification of other ESCRT-III proteins by western blotting as indicated on the left side of the panels. Lanes 1–3, input (2% of the lysate for co-purification; 20% of the lysate for Mos10–6His); lanes 4–6, Ni-NTA pulldown. The strains used were: JD52 (wild type, WT; lanes 1 and 4), RKY2889 (Mos10–6His; lanes 2 and 5), RKY3438 (Mos10–6His Δ*snf7*; lanes 3 and 6). The positions of tagged and native proteins are marked by arrows. Mos10–6His* indicates cross-reactivity of the Snf7 antiserum with Mos10–6His. (B) Western blot signals as described in A were quantified using ImageJ, and the percentage of co-purified ESCRT-III proteins was calculated (co-purification efficiency). Mean±s.d. of three independent experiments.

detection. The fusion proteins were expressed from single-copy plasmids under the control of the *PDC1* promoter (Fig. S8B). Depending on the TMs present in the N-terminal Vps68 fragment, the downstream sequences either point to the lumen of the ER or to the cytosol. When they point to the lumen of the ER, N-glycosylation sites in Suc2 are modified by the attachment of sugar chains, which leads to a mobility shift of the fusion protein on SDS gels. To prove that the mobility shift is caused by glycosylation, the sugar chains can be removed by endoglycosidase H (Endo H) treatment. The truncated His4C protein has histidinol dehydrogenase activity. Yeast cells expressing this protein are able to grow on histidinol plates in the absence of histidine in a *HOL1-1* strain background (Sengstag et al., 1990). This growth is only possible when His4C is present in the cytosol. Thus, we could use two complementary ways of assessing the localization of the sequences downstream of the Vps68 fragments.

The western blot analysis of the different fusion constructs is presented in Fig. 8A. The fusion protein without Vps68 sequences ran at the expected position of 114.3 kDa and was not affected by Endo H treatment. Insertion of the N-terminal Vps68 fragment containing TM1 led to a shift to higher mobility, larger than the one expected from the addition of the Vps68 sequences. This shift was reversed by Endo H treatment. This shows that TM1 spans the membrane and that the N terminus of Vps68 points to the cytosol, while the rest of the fusion protein is inside the ER. When a fragment containing TM1 and TM2 was inserted, the same pattern was obtained. This shows that TM2 does not span the membrane and that the sequences downstream of TM1 are still oriented towards the lumen of the ER. This fusion protein appeared to be unstable, because the western blot signal was weaker than the signal for the previous constructs. The same pattern was observed with the Vps68 fragment containing TM1, TM2 and TM3, indicating that TM3 also does not span the membrane. Finally, when the complete sequence of Vps68 containing all four TMs was inserted, no Endo H-dependent mobility shift was observed. This indicates that TM4 traverses the membrane and that the C terminus of Vps68 points to the cytosol. Next, the same strains were streaked out on plates containing either histidine or histidinol (Fig. 8B). While all strains grew on the histidine plate, only the fusion with full-length Vps68 and the control without Vps68 sequences were able to grow on the histidinol plate, indicating that in these constructs the His4C part localizes to the cytosol. This result is the exact mirror image of the western blot experiment. Taken together, these experiments demonstrate that Vps68 has indeed the same topology as Nce102. Vps68 forms a hairpin structure with TM1 and TM4 traversing the membrane and TM2 and TM3 being localized to the luminal side of the endosomal membrane (Fig. 8C). Both TM2 and TM3 appear to be AHs that are able to interact with the luminal leaflet of the endosomal membrane.

DISCUSSION

Here we present evidence that Vps68 interacts with ESCRT-III and that it cooperates with ESCRT-III in ILV formation and abscission. Our data further suggest that Snf7 could be replaced by Mos10 at some point in the ESCRT-III functional cycle. This switch in ESCRT-III subunits could be associated with a transition from an active complex to a disassembly-competent complex.

Vps68 interacts with ESCRT-III

In a previous report, it was proposed that Vps68 acts with or downstream of the ESCRT machinery to regulate a novel step in endosome biogenesis (Schluter et al., 2008). Our findings now

Journal of Cell Science (2022) 135, jcs259743. doi:10.1242/jcs.259743

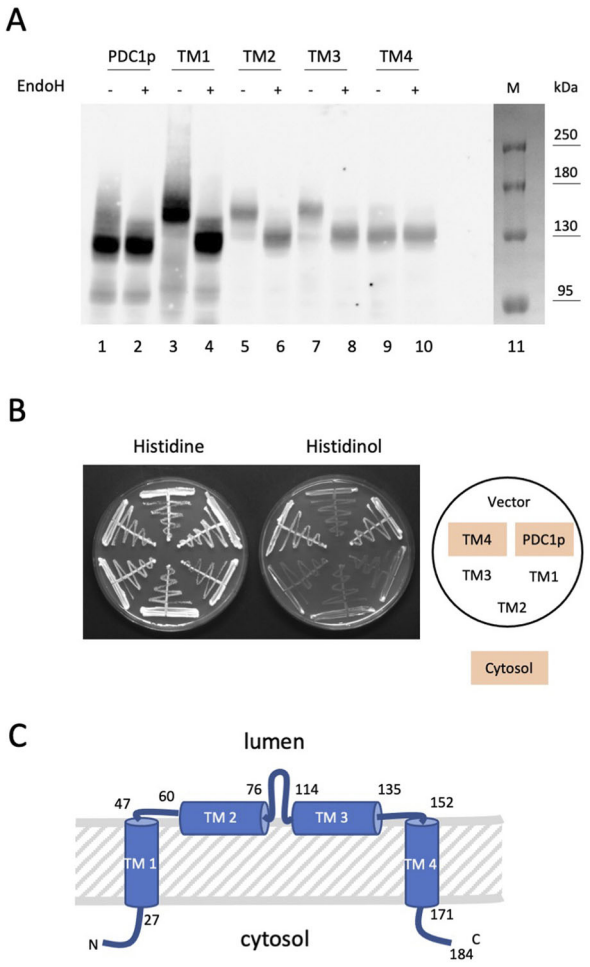

Fig. 8. Membrane topology of Vps68. The *HOL1-1* strain STY50 was transformed with plasmids expressing different fragments of Vps68 fused to Suc2 and His4C fragments. (A) Glycosylation patterns of fusion proteins. Cell extracts of the transformants were examined for the fusion proteins by western blotting with anti-HA antibodies. Cell extracts were either treated with Endo H to remove N-glycosylation (lanes with even numbers, Endo H +) or were left untreated (lanes with odd numbers, Endo H –). The following plasmids were used: pRK2015 (lanes 1 and 2, no Vps68; PDC1p, pyruvate decarboxylase 1), pRK2016 (lanes 3 and 4; TM1, Vps68 with TM1), pRK2017 (lanes 5 and 6; TM2, Vps68 with TM1 and TM2), pRK2018 (lanes 7 and 8; TM3, Vps68 with TM1, TM2 and TM3) and pRK2019 (lanes 9 and 10; TM4, full-length Vps68). Lane 11 shows protein markers (M) captured by white-light imaging and subsequently aligned with luminescence images of the same membrane. Blot is representative of two independent experiments. (B) Growth on histidinol plates. The transformants were plated on agar plates containing histidine (left) or histidinol (right). The plasmids contained in the transformants were (clockwise from top): YCplac33 (vector), pRK2015 (PDC1p), pRK2016 (TM1), pRK2017 (TM2), pRK2018 (TM3), pRK2019 (TM4). The plasmids expressing fusion proteins whose C-terminus points to the cytosol are highlighted in the diagram on the right. Data are representative of two independent experiments. (C) Membrane topology predicted from the experiments. The positions of the TMs in the Vps68 sequence are indicated.

suggest that Vps68 is tightly connected to ESCRT-III function. First of all, we were able to show that Vps68 physically interacts with ESCRT-III. At present it is not clear how Vps68 interacts with ESCRT-III, but Mos10 seems to be dispensable for the interaction, since ESCRT-III subunits could still be immunoprecipitated by Vps68 in the absence of Mos10. Loss of Vps68 leads to a shift in the composition of ESCRT-III. The number of core components in the complex (Snf7, Vps2 and Vps24) increases, while the number of the associated subunits (Did2, Ist1 and Mos10) decreases. This supports the view that at some point during the functional cycle a switch occurs from an active complex involved in ILV formation and/or abscission to a disassembly-competent complex. This switch is reflected in a change in ESCRT-III composition.

The precise function of ESCRT-III during the formation of an ILV is still not clear. ESCRT-III could be involved in the deformation of the endosomal membrane, or its function could be restricted to the release of the vesicle from the membrane into the lumen of the endosome. In any case, these events have to be tightly coordinated with the incorporation of cargo proteins into the forming vesicle. The function of ESCRT-III is completed when all cargo proteins are removed from the endosomal membrane. The cue that signals completion of the ESCRT-III task is not known, but it is tempting to speculate that the presence of ubiquitylated cargo proteins in the endosomal membrane is part of the signal. As soon as the ubiquitylated cargos are removed, ESCRT-III would switch to a disassembly-competent complex, followed by its rapid dissolution. The ESCRT-III-associated subunits have been implicated in ESCRT-III disassembly (Azmi et al., 2008; Dimaano et al., 2008; Rue et al., 2008). This notion is reinforced by our observation that ESCRT-III core components accumulate at the membrane in a *MOS10* deletion strain. The finding that the associated subunits are underrepresented in the Δ*vps68* strain, while the core subunits are overrepresented, indicates that the completion of the ESCRT-III task is delayed in Δ*vps68*. A close connection between Vp68 function and the presence of cargo protein is also suggested by our epistasis analysis. When the cargo protein Ste6–sfGFP was expressed to near wild-type levels, an effect of the *VPS68* deletion on the localization Ste6–sfGFP was barely detectable. Upon overexpression, however, a class E-like phenotype was observed. From this we conclude that Vps68 assists ESCRT-III in its function. When the load on the endocytic pathway is high, Vps68 is especially critical for the function of the ESCRT-III system.

Role of Vps68

What could be the role of Vps68? A potential function is suggested by the unusual membrane topology of the protein. We found that the two potential membrane helices 2 and 3 do not span the membrane but are instead localized to the luminal side of the endosomal membrane. At least helix 2 appears to be an AH with a hydrophilic and a hydrophobic face and a high hydrophobic moment. Helix 3 is probably also an AH. AHs have a tendency to interact with membrane surfaces. A number of functions have been ascribed to AHs (Gimenez-Andrés et al., 2018). The AH-containing protein Pex11, for instance, deforms membranes and induces tubulation. Some AHs can sense or stabilize membrane curvature – they act as amphipathic lipid-packing sensors. Yet other AHs, such as those in melittin, disturb the integrity of the lipid bilayer. We propose that Vps68, in a manner analogous to melittin, facilitates ILV abscission by disturbing the order of the lipids in the luminal leaflet of the bilayer. ESCRT-III in turn could act in the same way on the cytosolic leaflet. By simultaneously acting on opposing leaflets of the bilayer, ESCRT-III and Vps68 could promote the release of ILVs from the endosomal membrane.

Switch from a Snf7- to a Mos10-containing ESCRT-III complex?

As described above, it appears plausible that during an ESCRT-III functional cycle, a shift occurs from an active complex to a disassembly-competent complex. The shift is accompanied by a change in ESCRT-III composition. We think that the key event in

Journal of Cell Science (2022) 135, jcs259743. doi:10.1242/jcs.259743

this transition could be the replacement of Snf7 by Mos10. This conclusion is derived from our co-IP and pulldown experiments. In Ni-NTA pulldowns with Mos10–6His, the core ESCRT-III subunits Vps2 and Vps24 were co-purified but almost no Snf7. This is in line with a recent report, published as a preprint, where it was concluded that Mos10 forms a distinct ESCRT-III complex independent of Snf7 (Pfitzner et al., 2022 preprint). However, we do not think that these two complexes are completely independent of each other, because we could show that formation of the Mos10 complex depends on Snf7. Furthermore, both Snf7 and Mos10 are involved in the same process: ILV formation at endosomes. Considering the role of Mos10 in disassembly of ESCRT-III, our interpretation of these findings is that Snf7 initiates ESCRT-III formation but is replaced later on by Mos10, which then triggers disassembly.

Snf7 and Mos10 are closely related. The ESCRT-III proteins can be divided into two classes based on sequence homology (Leung et al., 2008). A member of each class was already present in the LCEA. The first class consists of Snf7, Mos10 and Vps20 (and also Chm7), and the second class contains Did2, Vps2 and Vps24. In fact, in our previous report, we were only able to identify the first class of ESCRT-III proteins; the second class escaped our attention due to divergence in the primary sequence (Kranz et al., 2001).

A number of observations suggest that Mos10 acts after Snf7. A previously published careful study of the morphology of MVBs in ESCRT-III mutants has shown a clear distinction between the core components Snf7, Vps2, Vps20 and Vps24 and the ESCRT-III-associated proteins Did2 and Mos10 (Nickerson et al., 2010). In that study, when one of the core components was deleted, no ILVs were formed. Instead, the typical class E structures – closely juxtaposed flattened endosomes – could be observed. In *did2* and *mos10* mutants, ILVs were stilled observed, but the MVBs formed structures with an elongated morphology called VTEs. Previous evidence and the findings in our study clearly point to a role of Mos10 in the disassembly of ESCRT-III, which appears to occur after ILV formation is finished.

Licensing in the endocytic pathway

Mos10–sfGFP showed a unique intracellular distribution. While the other ESCRT-III proteins localized to punctate structures, Mos10–sfGFP was detected at the vacuolar membrane. For the localization studies, we used C-terminally tagged ESCRT-III proteins. Most of these tagged proteins were compromised in their function. But still, useful information could be gained from the investigation of these proteins. The phenotypes of the tagged proteins were clearly different from those of complete knockouts, which shows that the function of these proteins is partly preserved. In fact, we think that these proteins can be used as tools to dissect the ESCRT-III cycle, since tagging of different ESCRT-III proteins arrests the cycle at distinct steps. Thus, tagging of Snf7 leads to an early arrest, while tagging of Mos10 arrests the cycle at a later time point. It appears that an early arrest, like the one imposed by tagging of Snf7, prevents downstream events such as tethering and fusion of late endosomes with the vacuolar membrane. For this reason, the tagged core ESCRT-III proteins were detected in endosomal structures and not at the vacuole. The successive events in the endocytic pathway seem to strictly depend on each other. Only upon successful completion of one step is the next step licensed. Thus, progression to endosome tethering only occurs when ILV formation is completed. Disassembly of ESCRT-III does not seem to be a precondition for endosome tethering to the vacuole. That is why the ESCRT-III complex containing Mos10–sfGFP was detected in endosomal structures tethered to the vacuole. ESCRT-III disassembly in turn could be a precondition for endosome fusion, since we observed a large number of Mos10–sfGFP structures at the vacuolar membrane. Mos10–sfGFP was not detected at the vacuolar membrane in a strain expressing tagged Snf7 or in a strain carrying a *VPS68* deletion. In these strains, Mos10–sfGFP showed an endosomal localization. This further supports the idea that Snf7 and Vps68 closely act together and that progression to endosome tethering is blocked when these functions are compromised.

MATERIALS AND METHODS

Plasmids and yeast strains

Yeast cells were grown in YPD medium (1% yeast extract, 2% peptone, 2% glucose) for immunoprecipitation experiments and in SD/CAS medium (0.67% yeast nitrogen base, 1% casamino acids, 2% glucose, 50 mg/l uracil and tryptophan) for fluorescence microscopy. For SILAC, yeasts were grown in SD medium (0.67% yeast nitrogen base, 2% glucose) with the required auxotrophic markers. Arginine and lysine labeled with heavy isotopes ($^{13}C_6$ and $^{15}N_2$) were obtained from Silantes GmbH (Munich, Germany). For the Gal-depletion experiment, cells were grown in YP medium with 2% galactose and 0.2% glucose. To initiate the chase, the cells were spun down and resuspended in YPD medium. For growth on histinidol, 6 mM histidinol (Sigma, St. Louis, MO, USA; H-6647) was added to SD agar plates supplemented with –His drop-out medium (Formedium, Hunstanton, UK, DSC0071). The yeast strains used are listed in Table S2. All yeast strains constructed in this study are derived from JD52 (Jürgen Dohmen, University of Cologne, Germany) by the integration of PCR cassettes into the yeast genome (Longtine et al., 1998). Some deletions were generated using the CRISPR/Cas9 technique (Brune et al., 2019). The plasmids used in this study are listed in Table S3.

Antibodies

Monoclonal antibodies against alkaline phosphatase were obtained from Invitrogen (Waltham, MA, USA; Thermo Fisher Scientific catalog # 459260, at a dilution of 1:1000). The anti-GFP antibody was obtained from Nordic-MUbio (Dianova, Hamburg, Germany, catalog # Bii-nGFPab4-100) and used at a dilution of 1:1000. All other antibodies were generated by immunization of rabbits, and details of their production, characterization and use have been described previously (Heinzle et al., 2019).

Mos10–6His purification by immobilized metal affinity chromatography

For SILAC experiments, cells were grown in SD medium with 50 mg/l adenine, histidine, uracil, tryptophan, 120 mg/l leucine and 60 mg/l arginine and lysine. Cells were grown overnight to exponential phase (OD_{600}<1.0) at 30°C, harvested and washed with phosphate-buffered saline (PBS). The wild-type strain RKY2998 was grown in light medium (containing unlabeled arginine and lysine) and the Mos10-6His strain RKY2999 was grown in heavy medium (containing arginine and lysine labeled with heavy isotopes). Equal amounts of cells grown in heavy or light medium were mixed and resuspended in 10 ml PBS. The cells were lysed by beating with glass beads in a Fast Prep24 machine (MP Biomedicals, Eschwege, Germany) (two times, 1 min, 4 m/s). Next, the cell lysate was incubated with 4 mM disuccinimidyl suberate (DSS) crosslinker (Thermo Fisher Scientific, Rockford, IL, USA) for 1 h at 4°C on a rocker. The reaction was stopped by quenching with 100 mM Tris-HCl pH 8, and the membranes were solubilized with 1% Triton X-100 for 15 min at 4°C. To remove cell debris, the lysate was spun at 15,000 ***g*** at 4°C for 15 min. The supernatant was adjusted to 300 mM NaCl and 15 mM imidazole, and then filtered through a 0.45 µm filter. The sample was then applied to an ÄKTA start chromatography system (GE Healthcare Europe GmbH, Freiburg, Germany), and purification of crosslinked proteins was achieved on a 1 ml HisTrap™ Fast Flow column (Cytiva, Marlborough, MA, USA, No. 17-5319-01). Bound proteins were eluted from the column by a 50–500 mM imidazole gradient. The collected fractions were analyzed by

SDS–PAGE with Coomassie Blue staining and western blotting with anti-Mos10 antibodies. The fractions containing Mos10–6His crosslinks were analyzed by mass spectrometry (Core Facility, University of Hohenheim). The MS was undertaken at the Core Facility in Hohenheim, Germany.

Mos10–6His was also purified by immobilized metal affinity chromatography on a small scale. Cells were grown in YPD medium to exponential phase, and 20 OD_{600} units of cells were harvested. The cells were processed as described below for the co-IP experiments, with the modification that after the 500 ***g*** spin, 20 mM imidazole and 50 µl of a 50% Ni-NTA bead slurry (Protino, Macherey-Nagel, Düren, Germany) were added instead of the antibodies and protein A sepharose beads.

Co-immunoprecipitation

For co-IP experiments, 50 OD_{600} units of cells from an exponential YPD culture were harvested, washed with PBS and resuspended in 200 µl PBS with protease inhibitors (in-house solution). The cells were lysed by beating with glass beads for 5 min at 4°C. After lysis, 600 µl PBS and 2.5 mM of the cleavable crosslinker dithiobis(succinimidyl propionate) (DSP; Thermo Fisher Scientific, Rockford, IL, USA) were added. The solution was incubated for 1 h at 4°C on a rocker. The crosslinking reaction was stopped by quenching with 100 mM Tris-HCl pH 8.0, and the membranes were dissolved using 1% Triton X-100. The reaction was incubated for 15 min at 4°C on a rocker and then centrifuged for 10 min at 500 ***g*** at 4°C to remove cell debris. Then, the supernatant was incubated with 10 µl antiserum for 1 h at 4°C on a rocker followed by an incubation with 80 µl of a 50% slurry of protein A sepharose beads (CL-4B, GE Healthcare, Uppsala, Sweden) for 1 h at 4°C. The solution was washed three times with 1 ml PBS at 100 g for 30 s. The beads were resuspended in a mixture of 100 µl PBS and 100 µl SDS sample buffer (60 mM Tris-HCl, 4% SDS, 20% glycerol, 0.01% Bromophenol Blue, 100 mM DTT) and heated to 95°C for 5 min.

Endoglycosidase H treatment

The cells were grown to exponential phase (OD_{600}<1) and 10 OD_{600} units of cells were harvested, washed in 10 mM NaN_3 and resuspended in 100 µl of lysis buffer (0.3 M sorbitol, 50 mM HEPES pH 7.5) with protease inhibitors (in-house solution). After lysis by beating with glass beads for 5 min at 4°C, 150 µl of SDS sample buffer was added, and then the mixture was heated at 50°C for 20 min. The lysate was centrifuged at 20,000 ***g*** for 5 min in a table-top centrifuge to remove cell debris. The supernatant was diluted 1:10 with Endo H buffer (50 mM Tris-HCl pH 6.8, 50 mM EDTA, 1% Triton X-100). Two 100 µl aliquots were incubated overnight at 37°C with and without Endo H (3000 U; NEB). Then the samples were heated with 100 µl SDS sample buffer for 5 min at 95°C.

Sucrose gradients

Yeast cultures were grown overnight in YPD medium (1% yeast extract, 2% peptone and 2% glucose) at 30°C to exponential phase. 50 OD_{600} units of cells were harvested, washed with 5 ml cold 10 mM NaN_3 and resuspended in 100 µl of STE10 lysis buffer [10% (w/w) sucrose, 10 mM Tris-HCl pH 7.6, 1 mM EDTA, 1 mM DTT and protease inhibitors (in-house solution)]. The cells were lysed by beating with glass beads for 5 min at 4°C. After addition of 500 µl of STE10 buffer, cell debris was removed by a 500 ***g*** spin for 10 min at 4°C. For gradient preparation, 1.7 ml of sucrose solutions with 53%, 36% and 20% sucrose (w/w) were layered on top of each other. The tubes were put in a horizontal position for 3 h to maximize diffusion between the layers. Then the tubes were put in a vertical position, generating a near-linear sucrose gradient. Next, 400 µl of cleared lysate was loaded on top of the gradient. The tubes were spun at 100,000 g_{av} for 16 h at 4°C in a Sorvall Discovery M120SE centrifuge with S52-ST rotor. Eighteen 280 µl fractions were collected from the top of the gradients and examined by western blotting.

Western blotting and live-cell imaging

Western blotting was performed according to standard protocols. For live-cell imaging, fluorochrome-tagged proteins were examined with an AXIO Imager.M1 with a Colibri 7 light source (Zeiss, Oberkochen, Germany). Images were captured with an Axiocam 506 mono digital camera. The cells were fixed to glass slides coated with a 0.6 mg/ml concanavalin A solution.

Acknowledgements

We thank Roger Schneiter for sending us the *HOL1-1* strain STY50.

Competing interests

The authors declare no competing or financial interests.

Author contributions

Conceptualization: R.K.; Methodology: S.A.; Validation: R.K.; Investigation: S.A., R.K.; Writing - original draft: R.K.; Writing - review & editing: R.K.; Supervision: R.K.; Funding acquisition: R.K.

Funding

This project was funded by the German Research Fund (Deutsche Forschungsgemeinschaft) KO 963/8-1 to R.K.

Peer review history

The peer review history is available online at https://journals.biologists.com/jcs/article-lookup/doi/10.1242/jcs.259743.

References

Adell, M. A. Y., Migliano, S. M., Upadhyayula, S., Bykov, Y. S., Sprenger, S., Pakdel, M., Vogel, G. F., Jih, G., Skillern, W., Behrouzi, R. et al. (2017). Recruitment dynamics of ESCRT-III and Vps4 to endosomes and implications for reverse membrane budding. *eLife* **6**, e31652. doi:10.7554/eLife.31652.037

Azmi, I., Davies, B., Dimaano, C., Payne, J., Eckert, D., Babst, M. and Katzmann, D. J. (2006). Recycling of ESCRTs by the AAA-ATPase Vps4 is regulated by a conserved VSL region in Vta1. *J. Cell Biol.* **172**, 705-717. doi:10.1083/jcb.200508166

Azmi, I. F., Davies, B. A., Xiao, J., Babst, M., Xu, Z. and Katzmann, D. J. (2008). ESCRT-III family members stimulate Vps4 ATPase activity directly or via Vta1. *Dev. Cell* **14**, 50-61. doi:10.1016/j.devcel.2007.10.021

Babst, M., Katzmann, D. J., Estepa-Sabal, E. J., Meerloo, T. and Emr, S. D. (2002). ESCRT-III: an endosome-associated heterooligomeric protein complex required for MVB sorting. *Dev. Cell* **3**, 271-282. doi:10.1016/S1534-5807(02)00220-4

Banjade, S., Tang, S., Shah, Y. H. and Emr, S. D. (2019). Electrostatic lateral interactions drive ESCRT-III heteropolymer assembly. *eLife* **8**, e46207. doi:10.7554/eLife.46207

Banjade, S., Shah, Y. H., Tang, S. and Emr, S. D. (2021). Design principles of the ESCRT-III Vps24-Vps2 module. *eLife* **10**, e67709. doi:10.7554/eLife.67709

Bauer, I., Brune, T., Preiss, R. and Kölling, R. (2015). Evidence for a non-endosomal function of the *Saccharomyces cerevisiae* ESCRT-III like protein Chm7. *Genetics* **201**, 1439-1452. doi:10.1534/genetics.115.178939

Bertin, A., de Franceschi, N., de la Mora, E., Maity, S., Alqabandi, M., Miguet, N., di Cicco, A., Roos, W. H., Mangenot, S., Weissenhorn, W. et al. (2020). Human ESCRT-III polymers assemble on positively curved membranes and induce helical membrane tube formation. *Nat. Commun.* **11**, 2663. doi:10.1038/s41467-020-16368-5

Bonangelino, C. J., Chavez, E. M. and Bonifacino, J. S. (2002). Genomic screen for vacuolar protein sorting genes in Saccharomyces cerevisiae. *Mol. Biol. Cell* **13**, 2486-2501. doi:10.1091/mbc.02-01-0005

Bowers, K. and Stevens, T. H. (2005). Protein transport from the late Golgi to the vacuole in the yeast Saccharomyces cerevisiae. *Biochim. Biophys. Acta* **1744**, 438-454. doi:10.1016/j.bbamcr.2005.04.004

Brune, T., Kunze-Schumacher, H. and Kölling, R. (2019). Interactions in the ESCRT-III network of the yeast Saccharomyces cerevisiae. *Curr. Genet.* **65**, 607-619. doi:10.1007/s00294-018-0915-8

Chiaruttini, N., Redondo-Morata, L., Colom, A., Humbert, F., Lenz, M., Scheuring, S. and Roux, A. (2015). Relaxation of loaded ESCRT-III spiral springs drives membrane deformation. *Cell* **163**, 866-879. doi:10.1016/j.cell.2015.10.017

Dimaano, C., Jones, C. B., Hanono, A., Curtiss, M. and Babst, M. (2008). Ist1 regulates Vps4 localization and assembly. *Mol. Biol. Cell* **19**, 465-474. doi:10.1091/mbc.e07-08-0747

Gatta, A. T. and Carlton, J. G. (2019). The ESCRT-machinery: closing holes and expanding roles. *Curr. Opin. Cell Biol.* **59**, 121-132. doi:10.1016/j.ceb.2019.04.005

Gimenez-Andrés, M., Čopič, A. and Antonny, B. (2018). The many faces of amphipathic helices. *Biomolecules* **8**, 45. doi:10.3390/biom8030045

Heinzle, C., Mücke, L., Brune, T. and Kölling, R. (2019). Comprehensive analysis of yeast ESCRT-III composition in single ESCRT-III deletion mutants. *Biochem. J.* **476**, 2031-2046. doi:10.1042/BCJ20190141

Huh, W.-K., Falvo, J. V., Gerke, L. C., Carroll, A. S., Howson, R. W., Weissman, J. S. and O'Shea, E. K. (2003). Global analysis of protein localization in budding yeast. *Nature* **425**, 686-691. doi:10.1038/nature02026

Hurley, J. H. (2015). ESCRTs are everywhere. *EMBO J.* **34**, 2398-2407. doi:10.15252/embj.201592484

Junglas, B., Huber, S. T., Heidler, T., Schlösser, L., Mann, D., Hennig, R., Clarke, M., Hellmann, N., Schneider, D. and Sachse, C. (2021). PspA adopts an ESCRT-III-like fold and remodels bacterial membranes. *Cell* **184**, 3674-3688.e18. doi:10.1016/j.cell.2021.05.042

Kölling, R. and Hollenberg, C. P. (1994). The ABC-transporter Ste6 accumulates in the plasma membrane in a ubiquitinated form in endocytosis mutants. *EMBO J.* **13**, 3261-3271. doi:10.1002/j.1460-2075.1994.tb06627.x

Kranz, A., Kinner, A. and Kölling, R. (2001). A family of small coiled-coil-forming proteins functioning at the late endosome in yeast. *Mol. Biol. Cell* **12**, 711-723. doi:10.1091/mbc.12.3.711

Krsmanović, T., Pawelec, A., Sydor, T. and Kölling, R. (2005). Control of Ste6 recycling in the early endocytic pathway in yeast. *Mol. Biol. Cell* **16**, 2809-2821. doi:10.1091/mbc.e04-10-0941

Langemeyer, L., Borchers, A.-C., Herrmann, E., Füllbrunn, N., Han, Y., Perz, A., Auffarth, K., Kümmel, D. and Ungermann, C. (2020). A conserved and regulated mechanism drives endosomal Rab transition. *eLife* **9**, e56090. doi:10.7554/eLife.56090

Lee, I. H., Kai, H., Carlson, L. A., Groves, J. T. and Hurley, J. H. (2015). Negative membrane curvature catalyzes nucleation of endosomal sorting complex required for transport (ESCRT)-III assembly. *Proc. Natl. Acad. Sci. USA* **112**, 15892-15897. doi:10.1073/pnas.1518765113

Leung, K. F., Dacks, J. B. and Field, M. C. (2008). Evolution of the multivesicular body ESCRT machinery; retention across the eukaryotic lineage. *Traffic* **9**, 1698-1716. doi:10.1111/j.1600-0854.2008.00797.x

Liu, J., Tassinari, M., Souza, D. P., Naskar, S., Noel, J. K., Bohuszewicz, O., Buck, M., Williams, T. A., Baum, B. and Low, H. H. (2021). Bacterial Vipp1 and PspA are members of the ancient ESCRT-III membrane-remodeling superfamily. *Cell* **184**, 3660-3673.e18. doi:10.1016/j.cell.2021.05.041

Loibl, M., Grossmann, G., Stradalova, V., Klingl, A., Rachel, R., Tanner, W., Malinsky, J. and Opekarová, M. (2010). C terminus of Nce102 determines the structure and function of microdomains in the Saccharomyces cerevisiae plasma membrane. *Eukaryot. Cell* **9**, 1184-1192. doi:10.1128/EC.00006-10

Longtine, M. S., McKenzie, A., Demarini, D. J., Shah, N. G., Wach, A., Brachat, A., Philippsen, P. and Pringle, J. R. (1998). Additional modules for versatile and economical PCR-based gene deletion and modification in *Saccharomyces cerevisiae*. *Yeast* **14**, 953-961.

Maity, S., Caillat, C., Miguet, N., Sulbaran, G., Effantin, G., Schoehn, G., Roos, W. H. and Weissenhorn, W. (2019). VPS4 triggers constriction and cleavage of ESCRT-III helical filaments. *Sci. Adv.* **5**, eaau7198. doi:10.1126/sciadv.aau7198

McCullough, J., Frost, A. and Sundquist, W. I. (2018). Structures, functions, and dynamics of ESCRT-III/Vps4 membrane remodeling and fission complexes. *Annu. Rev. Cell Dev. Biol.* **34**, 85-109. doi:10.1146/annurev-cellbio-100616-060600

Mellacheruvu, D., Wright, Z., Couzens, A. L., Lambert, J. P., St-Denis, N. A., Li, T., Miteva, Y. V., Hauri, S., Sardiu, M. E., Low, T. Y. et al. (2013). The CRAPome: a contaminant repository for affinity purification-mass spectrometry data. *Nat. Methods* **10**, 730-736. doi:10.1038/nmeth.2557

Mierzwa, B. E., Chiaruttini, N., Redondo-Morata, L., von Filseck, J. M., König, J., Larios, J., Poser, I., Müller-Reichert, T., Scheuring, S., Roux, A. et al. (2017). Dynamic subunit turnover in ESCRT-III assemblies is regulated by Vps4 to mediate membrane remodelling during cytokinesis. *Nat. Cell Biol.* **19**, 787-798. doi:10.1038/ncb3559

Nickerson, D. P., West, M. and Odorizzi, G. (2006). Did2 coordinates Vps4-mediated dissociation of ESCRT-III from endosomes. *J. Cell Biol.* **175**, 715-720. doi:10.1083/jcb.200606113

Nickerson, D. P., West, M., Henry, R. and Odorizzi, G. (2010). Regulators of Vps4 ATPase activity at endosomes differentially influence the size and rate of formation of intralumenal vesicles. *Mol. Biol. Cell* **21**, 1023-1032. doi:10.1091/mbc.e09-09-0776

Pfitzner, A. K., Mercier, V., Jiang, X., Moser von Filseck, J., Baum, B., Šarić, A. and Roux, A. (2020). An ESCRT-III polymerization sequence drives membrane deformation and fission. *Cell* **182**, 1140-1155.e18. doi:10.1016/j.cell.2020.07.021

Pfitzner, A. K., Zivkovic, H., Humbert, F. and Roux, A. (2022). Vps60 initiates formation of alternative membrane-bound ESCRT-III filaments. *bioRxiv*. doi:10.1101/2022.02.16.480668

Raymond, C. K., Howald, S. I., Vater, C. A. and Stevens, T. H. (1992). Morphological classification of the yeast vacuolar protein sorting mutants: evidence for a prevacuolar compartment in class E *vps* mutants. *Mol. Biol. Cell* **3**, 1389-1402. doi:10.1091/mbc.3.12.1389

Rue, S. M., Mattei, S., Saksena, S. and Emr, S. D. (2008). Novel Ist1-Did2 complex functions at a late step in multivesicular body sorting. *Mol. Biol. Cell* **19**, 475-484. doi:10.1091/mbc.e07-07-0694

Schluter, C., Lam, K. K., Brumm, J., Wu, B. W., Saunders, M., Stevens, T. H., Bryan, J. and Conibear, E. (2008). Global analysis of yeast endosomal transport identifies the vps55/68 sorting complex. *Mol. Biol. Cell* **19**, 1282-1294. doi:10.1091/mbc.e07-07-0659

Sengstag, C., Stirling, C., Schekman, R. and Rine, J. (1990). Genetic and biochemical evaluation of eucaryotic membrane protein topology: multiple transmembrane domains of Saccharomyces cerevisiae 3-hydroxy-3-methylglutaryl coenzyme A reductase. *Mol. Cell. Biol.* **10**, 672-680. doi:10.1128/MCB.10.2.672

Tang, S., Henne, W. M., Borbat, P. P., Buchkovich, N. J., Freed, J. H., Mao, Y., Fromme, J. C. and Emr, S. D. (2015). Structural basis for activation, assembly and membrane binding of ESCRT-III Snf7 filaments. *eLife* **4**, e12548. doi:10.7554/eLife.12548

Teis, D., Saksena, S. and Emr, S. D. (2008). Ordered assembly of the ESCRT-III complex on endosomes is required to sequester cargo during MVB formation. *Dev. Cell* **15**, 578-589. doi:10.1016/j.devcel.2008.08.013

Thaller, D. J., Allegretti, M., Borah, S., Ronchi, P., Beck, M. and Lusk, C. P. (2019). An ESCRT-LEM protein surveillance system is poised to directly monitor the nuclear envelope and nuclear transport system. *Elife* **8**, e12548. doi:10.7554/eLife.45284

Vietri, M., Radulovic, M. and Stenmark, H. (2020). The many functions of ESCRTs. *Nat. Rev. Mol. Cell Biol.* **21**, 25-42. doi:10.1038/s41580-019-0177-4

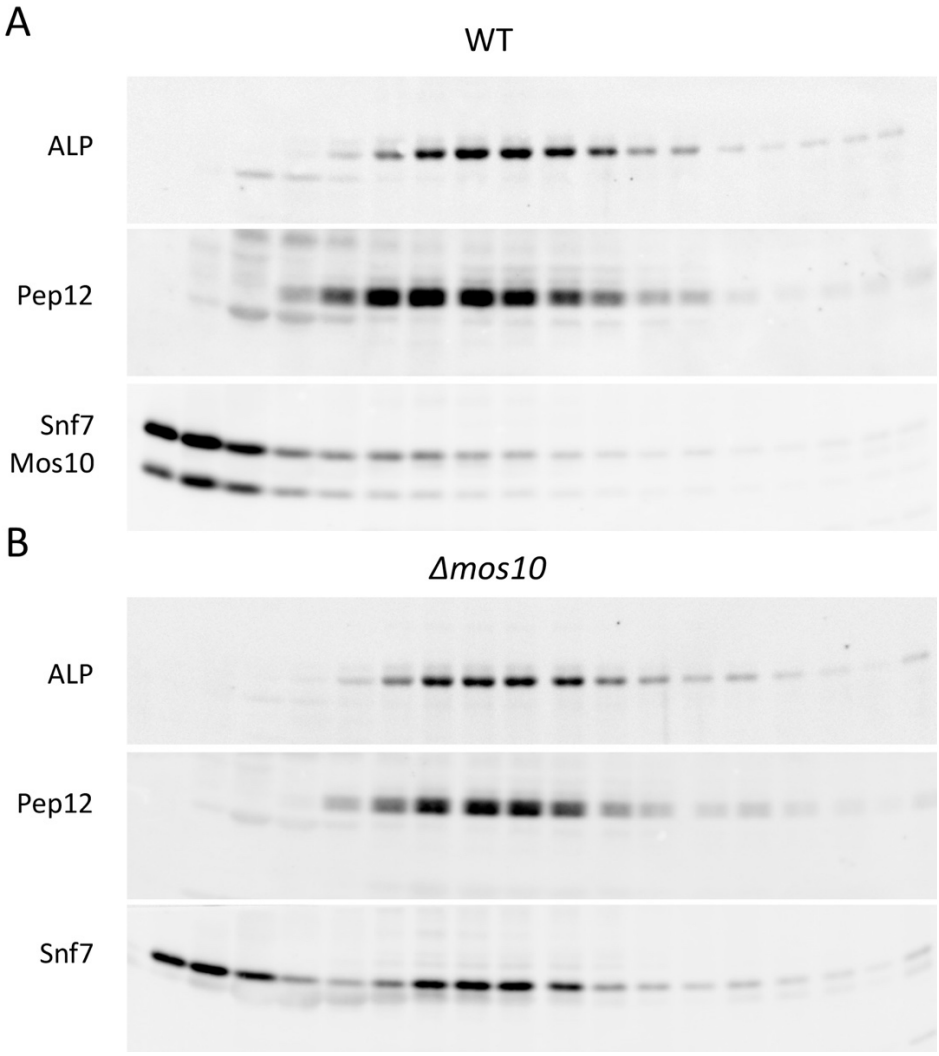

Fig. S1. Membrane accumulation of Snf7 in a *MOS10* deletion mutant. Western blots to Fig. 1. (A) RKY1558 (WT), (B) RKY2909 (*Δmos10*), proteins (from top to bottom): alkaline phosphatase (ALP), Pep12, Snf7/Mos10.

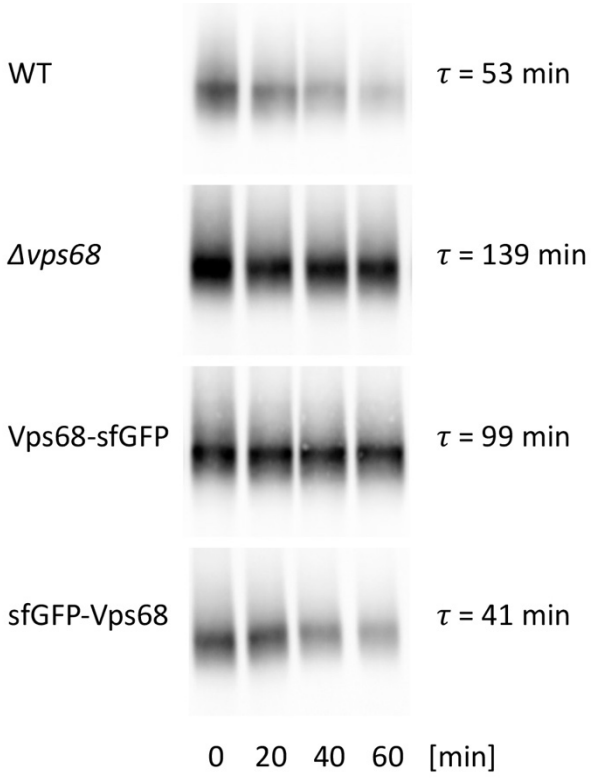

Fig. S2. Ste6 turnover. Cycloheximide chase. Yeast cells were grown in YPD medium. At t_0 100 µg/ml cycloheximide were added. Cell extracts of equal volumes of the culture were prepared at the times indicated and examined for Ste6 by western blotting. Strains (from top to bottom): RKY1558 (wildtype), RKY3222 (*Δvps68*), RKY3183 (*VPS68-sfGFP*), RKY3285 (*sfGFP-VPS68*). The signals were quantified by ImageJ and the Ste6 half-lives were calculated (as indicated). Ste6 half-lives were higher with CHX than in the gal depletion experiment, due to inhibitory effects of CHX on endocytic trafficking.

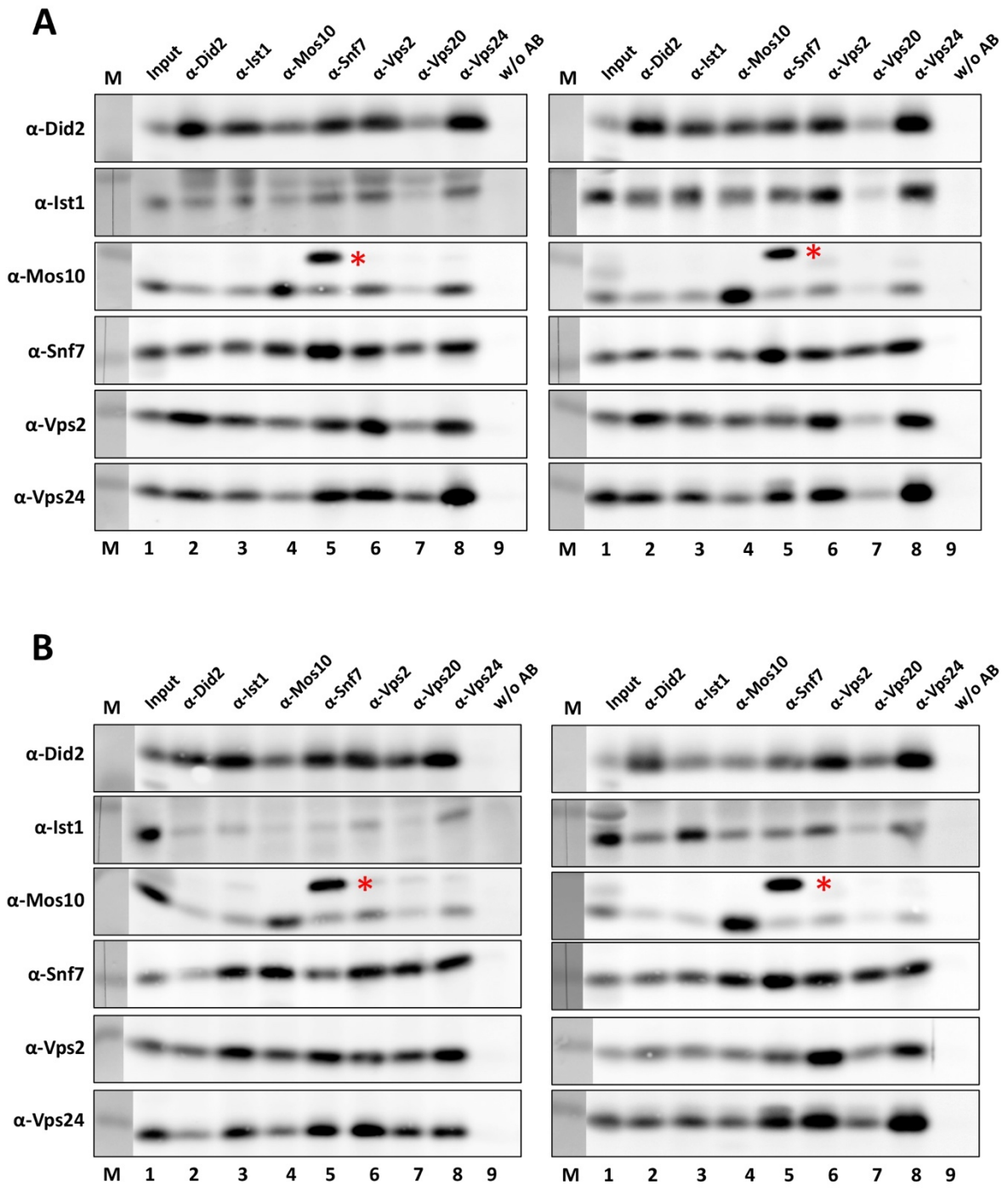

Fig. S3. Co-immunoprecipitation of ESCRT-III proteins. ESCRT-III proteins were immunoprecipitated from cell extracts with specific antibodies. The antibodies used for the primary IP are indicated on top of the diagrams (lanes 2-8). Lane 1: input, lane 9: negative control, IP reaction without antibodies, M: protein marker. The immunoprecipitates were examined for co-immunoprecipitation of other ESCRT-III proteins by western blotting with the antibodies indicated on the left side of the diagrams. (A) JD52 (wildtype), (B) RKY3222 *(Δvps68)*, two independent experiments each. *Cross-reactivity of anti-Mos10 with Snf7. The marker lanes were captured by white-light imaging and subsequently aligned with luminescence images of the same membrane. The thin black lines in some of the marker lanes are the result of the membrane being cut during blot processing.

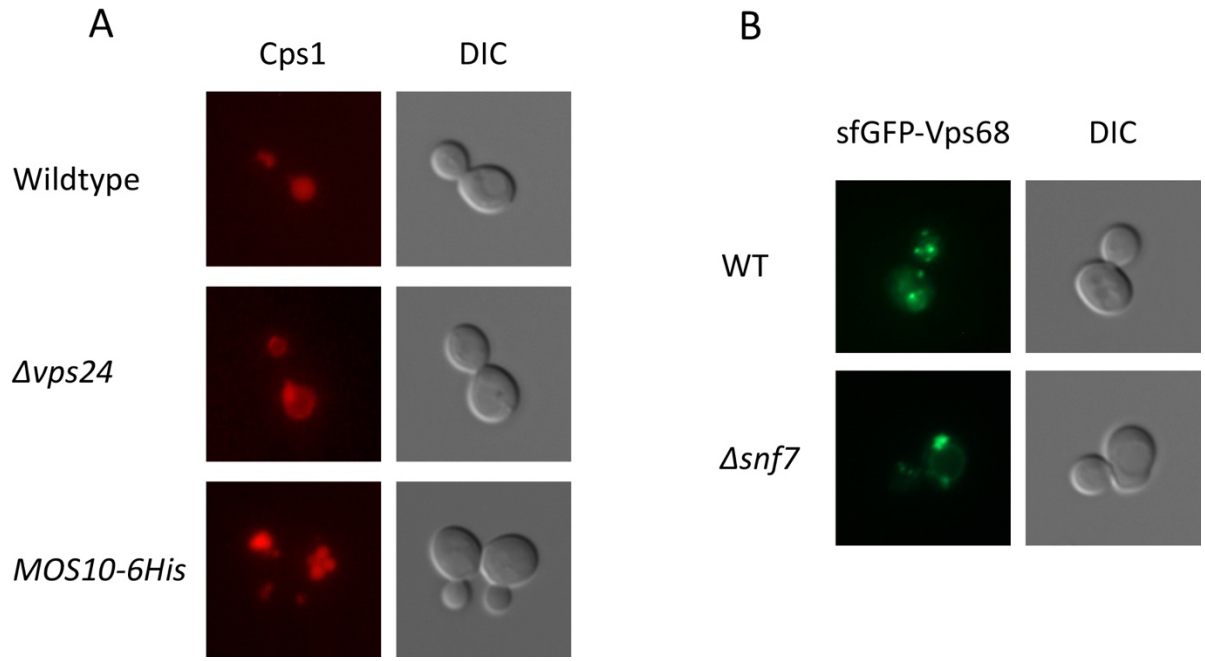

Fig. S4. (A) Test for functionality of ESCRT-III-sfGFP fusions, controls. Different yeast strains were transformed with the centromere plasmid pRK1408 expressing mCherry-Cps1 from the *HXT7* promoter. Left panels: mCherry-Cps1 fluorescence, right panels: DIC (B) Localization of sfGFP-Vps68. Strains, top: RKY3285 (*sfGFP-VPS68*), bottom: RKY3412 (*sfGFP-VPS68 Δsnf7*). Left panels: sfGFP-Vps68 fluorescence, right panels: DIC image.

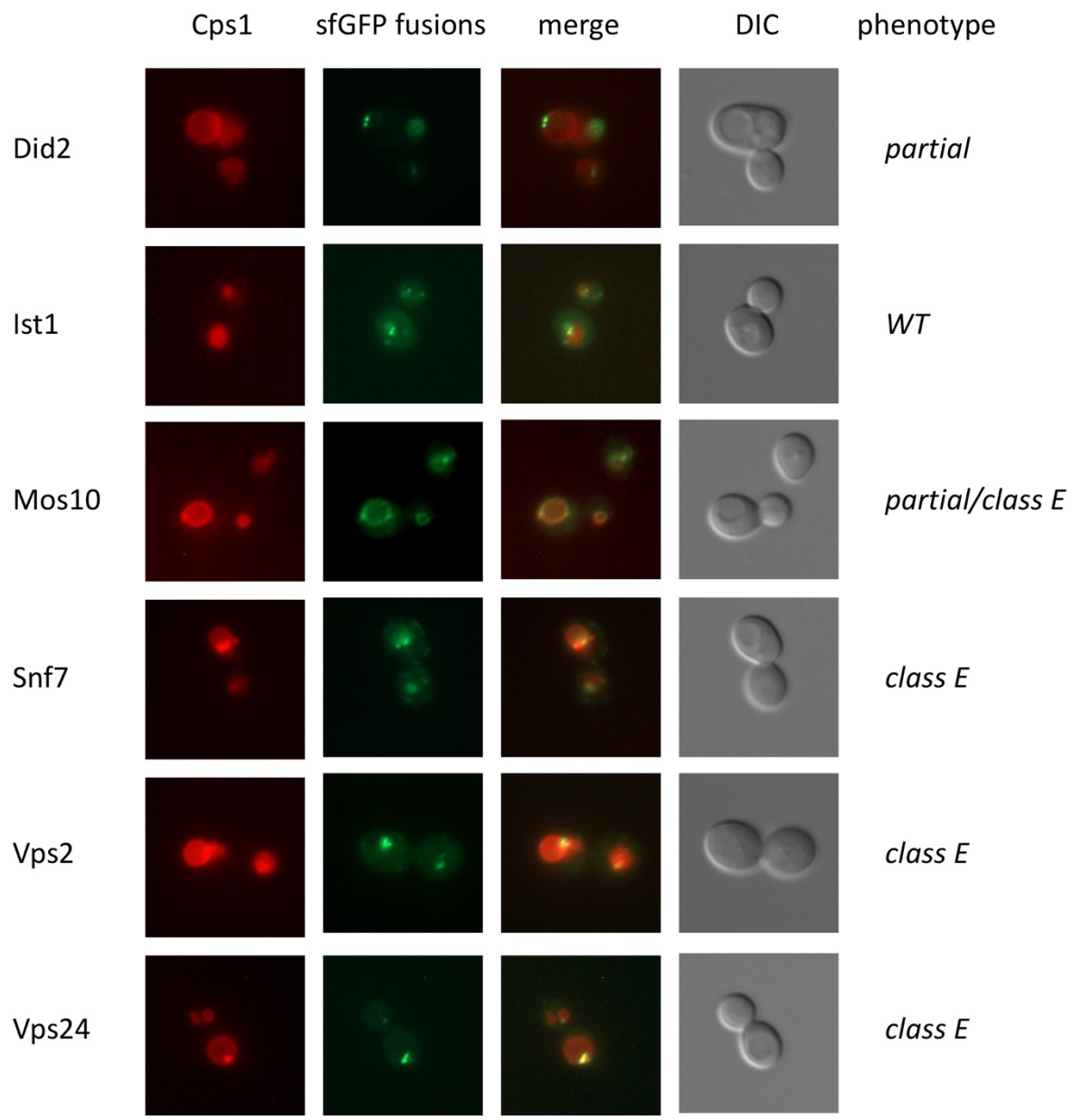

Fig. S5. Test for functionality of ESCRT-III-sfGFP fusions. Yeast strains expressing ESCRT-III-sfGFP fusions from their chromosomal loci were transformed with the centromere plasmid pRK1408 expressing mCherry-Cps1 from the *HXT7* promoter. Panels from left to right: mCherry-Cps1 fluorescence, ESCRT-III-sfGFP fluorescence, merged image, DIC image. Strains from top to bottom: RKY3214 (Did2-sfGFP), RKY3215 (Ist1-sfGFP), RKY3216 (Mos10-sfGFP), RKY3217 (Snf7-sfGFP), RKY3218 (Vps2-sfGFP), RKY3220 (Vps24-sfGFP). The Cps1 sorting phenotype is indicated on the right side of the figure.

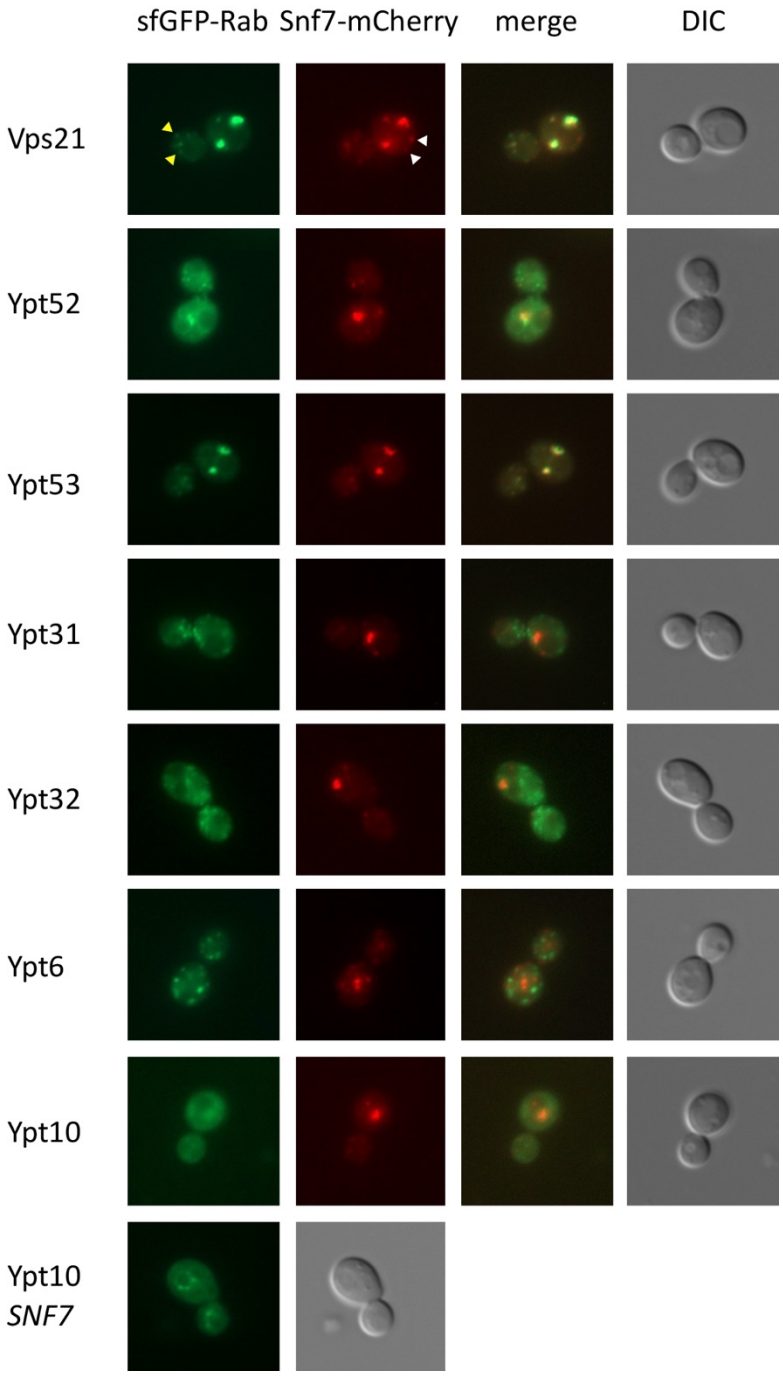

Fig. S6. Co-localization of sfGFP-Rab proteins with Snf7-mCherry. Yeast strains expressing N-terminally tagged sfGFP-Rab proteins and C-terminally tagged Snf7-mCherry from their chromosomal loci were examined by fluorescence microscopy. Panels from left to right: sfGFP-Rab fluorescence, Snf7-mCherry fluorescence, merged image, DIC image. Strains from top to bottom (all expressing Snf7-mCherry): RKY3423 (sfGFP-Vps21), RKY3425 (sfGFP-Ypt52), RKY3361 (sfGFP-Ypt53), RKY3362 (sfGFP-Ypt31), RKY3363 (sfGFP-Ypt32), RKY3364 (sfGFP-Ypt6), RKY3365 (sfGFP-Ypt10). Bottom panels: RKY3351 (sfGFP-Ypt10 without Snf7-mCherry, only GFP fluorescence and DIC image are shown). Arrows in Vps21 panel, yellow: sfGFP-Vps21 only, white: Snf7-mCherry only.

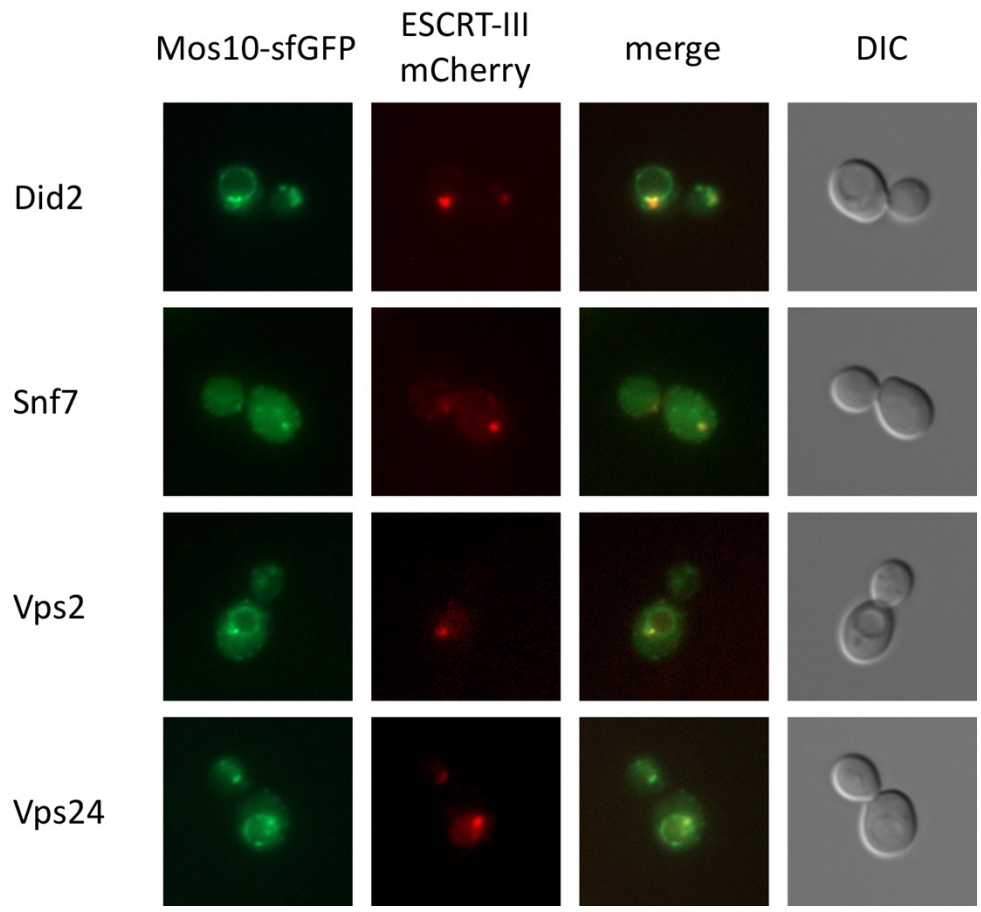

Fig. S7. Co-localization of Mos10-sfGFP with ESCRT-III-mCherry fusions. Yeast strains expressing Mos10-sfGFP and ESCRT-III-mCherry fusions from their chromosomal loci were examined for co-localization by fluorescence microscopy. Panels from left to right: Mos10-sfGFP fluorescence, ESCRT-III-mCherry fluorescence, merged image, DIC image. Strains from top to bottom (all expressing Mos10-sfGFP): RKY3481 (Did2-mCherry), RKY3459 (Snf7-mCherry), RKY3461 (Vps2-mCherry), RKY3462 (Vps24-mCherry).

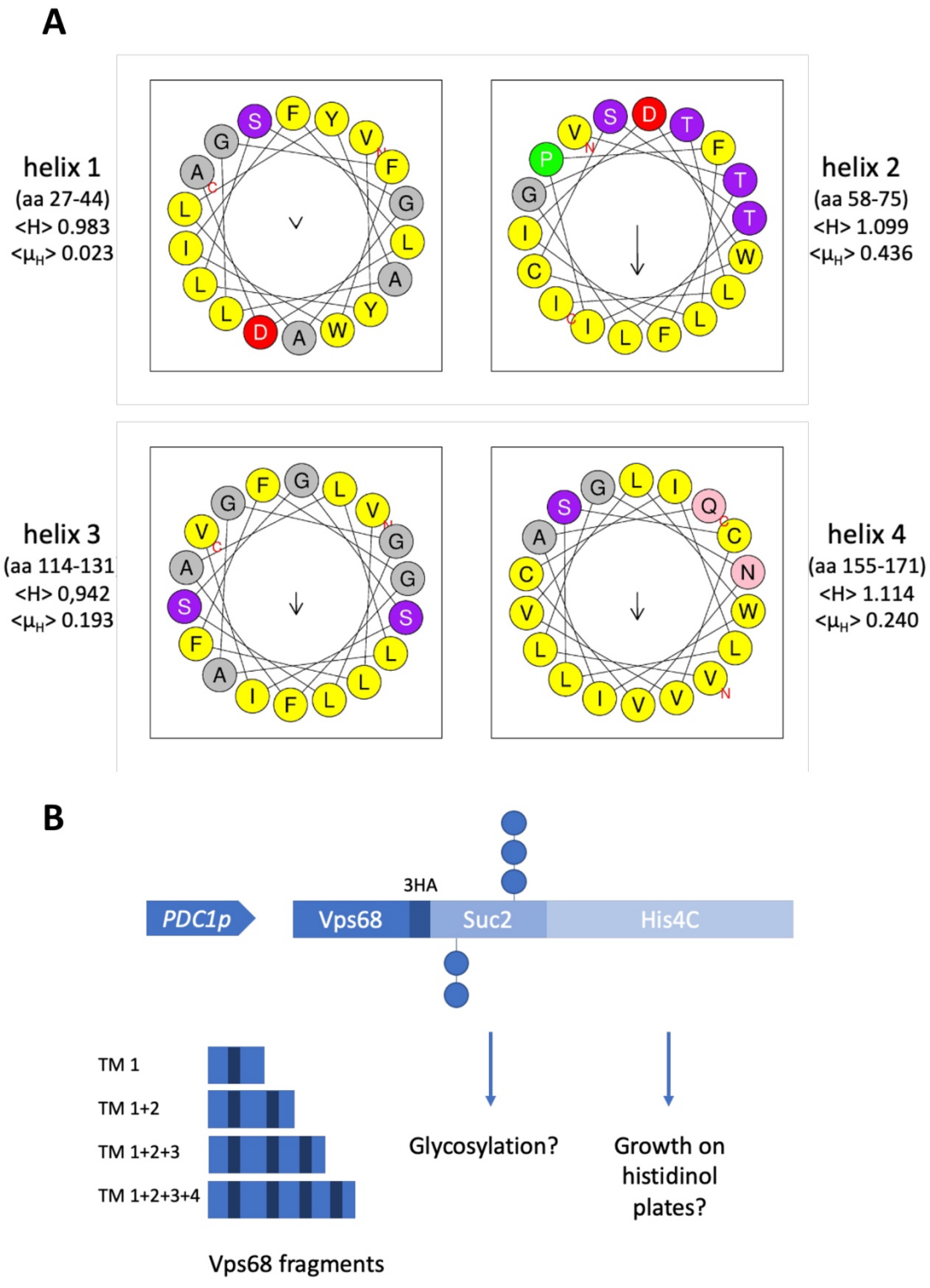

Fig. S8. (A) Helical wheel projection of the predicted TMs of Vps68. The predicted TMs of Vps68 were analyzed with HeliQuest (Gautier*etal*, 2008). The hydrophobicity (<H>) and the hydrophobic moment (<μ_H>) are indicated for each α-helix. (B) Vps68 topology reporter. A schematic representation of the fusion proteins used to study the Vps68 topology (see text).

Table S1. Mos10 interacting proteins identified by SILAC/MS (n=3)

Protein	CRAPome*	H/L ratio		
VPS60	**0 / 17**	**115.8**	**13.7**	**13.0**
TPS1	0 / 17	22.4		
COG8	1 / 17	11.1		
MSS1	0 / 17	11.0		
VPS2	**0 / 17**	**10.6**	**10.5**	**8.2**
RPS3	*17 / 17*	*9.7*		
TAF7	0 / 17	9.2		
SNF7	**0 / 17**	**8.8**	**8.2**	**7.4**
PRE6	2 / 17	7.8		
VPS24	**0 / 17**	**7.7**	**4.0**	**2.6**
NTH1	0 / 17	7.7		
EXO84	1 / 17	6.5		
FKS1	*7 / 17*	*5.7*		
SSB1	*17 / 17*	*5.7*		
VMA5	4 / 17	5.5		
VPS68	**0 / 17**	**4.8**		
DID2	**0 / 17**	**4.5**	**4.2**	
ARP3	1 / 17	4.5		
DNF2	1 / 17	4.1		
HEF3	*8 / 17*	*3.9*		
NEW1	*11 / 17*	*3.6*		
YKR075C[+]	0 / 17	3.6		
YGR130C	0 / 17	3.3		
RPL9B, RPL9A	*17 / 17*	*3.2*		
RTS1	0 / 17	3.2		
YCK2	1 / 17	3.1		
OAC1	0 / 17	2.9	2.3	
CBK1	4 / 17	2.9		
PTR2	0 / 17	2.9		
ALD5	1 / 17	2.8		
LEU1	1 / 17	2.7		
HBT1	0 / 17	2.5	2.3	
HHT1	*11 / 17*	*2.5*		
MNN5	0 / 17	2.5		
PAN1	1 / 17	2.5		
PMA1, PMA2	*17 / 17*	*2.5*		
FRT2	0 / 17	2.4		
HXK1, HXK2	*6 / 17*	*2.4*		
YTA12	0 / 17	2.4		
BAG7[+]	0 / 17	2.3		
CDC28	0 / 17	2.3		
STB6	0 / 17	2.3		

HXT1	0 / 17	2.2		
TDH1	*12 / 17*	*2.2*		
TIM10	1 / 17	2.2		
TYA	n.a.	2.2		
COX4	0 / 17	2.1		
TOM71	0 / 17	2.1		
YCK1	0 / 17	2.1		
ILV5	*6 / 17*	*2.0*		
SSE2	*5 / 17*	*2.0*		
YAT2	0 / 17	2.0		

ESCRT-III proteins and Vps68 in bold print

*The CRAPome: a Contaminant Repository for Affinity Purification Mass Spectrometry Data. Mellacheruvu et al. (2013) Nature Methods 10, 730–736

CRAPome > 4/17 (detected 4-times or more in 17 purifications) highlighted

$^{+}$Poly-His Proteins

Table S2. Yeast strains

Strain	Genotype	
RKY1558, alias JD52	*MATa ura3-52 his3-Δ200 leu2-3,112 trp1-Δ63 lys2-801 ssd1-d2*	J. Dohmen, Köln
STY50	*MATα his4-401 leu2-3,112 trp1-1 ura3-52 HOL1-1*	R. Schneiter, Fribourg
RKY 1920	*MATa Δvps21::LEU2*	this study
RKY 2790	*MATa Δsnf7*	this study
RKY 2830	*MATa Δvps24*	this study
RKY 2889	*MATa MOS10-6His::His3*	this study
RKY 2909	*MATa Δmos10::His3*	this study
RKY 2978	*MATa SNF7-6His::His3*	this study
RKY 2998	*MATa Δarg4*	this study
RKY 2999	*MATa Δarg4 MOS10-6His::His3*	this study
RKY 3183	*MATa VPS68-sfGFP::kan*	this study
RKY 3210	*MATa Δarg4 MOS10-sfGFP::kan*	this study
RKY 3214	*MATa DID2-sfGFP::kan*	this study
RKY 3215	*MATa IST1-sfGFP::kan*	this study
RKY 3216	*MATa MOS10-sfGFP::kan*	this study
RKY 3217	*MATa SNF7-sfGFP::kan*	this study
RKY 3218	*MATa VPS2-sfGFP::kan*	this study
RKY 3220	*MATa VPS24-sfGFP::kan*	this study
RKY 3222	*MATa Δvps68::kan*	this study
RKY 3224	*MATa MOS10-sfGFP::kan Δvps68::His3*	this study
RKY 3257	*MATa IST1-sfGFP::His3 Δvps68::kan*	this study
RKY 3269	*MATa DID2-sfGFP::kan Δvps68::His3*	this study
RKY 3271	*MATa VPS2-sfGFP::kan Δvps68::His3*	this study
RKY 3274	*MATa VPS24-sfGFP::kan Δvps68::His3*	this study
RKY 3279	*MATa SNF7-sfGFP::kan Δvps68::His3*	this study
RKY 3285	*MATa vps68::[kan SNF7p-sfGFP-VPS68]*	this study
RKY 3300	*MATa Δsnf7 Δvps68::kan*	this study
RKY 3307	*MATa Δvps21::LEU2 Δvps68::kan*	this study
RKY 3319	*MATa ste6::[kan GAL1p-STE6]*	this study
RKY 3320	*MATa Δvps68::kan ste6::[His3 GAL1p-STE6]*	this study

RKY 3351	*MATa ypt10::[His3 SNF7p-sfGFP-YPT10]*	this study
RKY 3361	*MATa SNF7-mCherry::kan ypt53::[His3 SNF7p-sfGFP-YPT53]*	this study
RKY 3362	*MATa SNF7-mCherry::kan ypt31::[His3 SNF7p-sfGFP-YPT31]*	this study
RKY 3363	*MATa SNF7-mCherry::kan ypt32::[His3 SNF7p-sfGFP-YPT32]*	this study
RKY 3364	*MATa SNF7-mCherry::kan ypt6::[His3 SNF7p-sfGFP-YPT6]*	this study
RKY 3365	*MATa SNF7-mCherry::kan ypt10::[His3 SNF7p-sfGFP-YPT10]*	this study
RKY 3376	*MATa Δvps21::LEU2 Δsnf7::kan*	this study
RKY 3384	*MATa DID2-mCherry::kan SNF7-sfGFP::His*	this study
RKY 3394	*MATa vps68::[kan SNF7p-sfGFP-VPS68] Δmos10::His3*	this study
RKY 3412	*MATa vps68::[kan SNF7p-sfGFP-VPS68] Δsnf7::His3*	this study
RKY 3423	*MATa SNF7-mCherry::kan vps21::[His3 SNF7p-sfGFP-VPS21]*	this study
RKY 3425	*MATa SNF7-mCherry::kan ypt52::[His3 SNF7p-sfGFP-YPT52]*	this study
RKY 3429	*MATa MOS10-sfGFP::kan SEC63-mCherry::His3*	this study
RKY 3437	*MATa MOS10-sfGFP::kan Δvps20::His3*	this study
RKY 3438	*MATa MOS10-6His::His3 Δsnf7::kan*	this study
RKY 3448	*MATa MOS10-sfGFP::kan VPH1-mCherry::His3*	this study
RKY 3458	*MATa MOS10-sfGFP::kan Δsnf7::His3*	this study
RKY 3459	*MATa MOS10-sfGFP::kan SNF7-mCherry::His3*	this study
RKY 3461	*MATa MOS10-sfGFP::kan VPS2-mCherry::His3*	this study
RKY 3462	*MATa MOS10-sfGFP::kan VPS24-mCherry::His3*	this study
RKY 3473	*MATa MOS10-mCherry::kan vps21::[His3 SNF7p-sfGFP-VPS21]*	this study
RKY 3478	*MATa MOS10-sfGFP::kan Δdid2::His3*	this study
RKY 3479	*MATa MOS10-sfGFP::kan Δvps2::His3*	this study
RKY 3481	*MATa MOS10-sfGFP::His3 DID2-mCherry::kan*	this study
RKY 3482	*MATa MOS10-mCherry::His3 COG5-sfGFP::kan*	this study
RKY 3484	*MATa MOS10-mCherry::His3 cps1::[kan SNF7p-sfGFP-CPS1]*	this study
RKY 3486	*MATa MOS10-mCherry::His3 STE6-sfGFP::kan*	this study
RKY 3490	*MATa MOS10-sfGFP::kan Δvps24*	this study

Table S3. Plasmids

Plasmid	Insert	Vector*	Replicon, Marker
pRK599	STE6-GFP	YEplac195	2µ, URA3
pRK1408	HXT7p-mCherry-CPS1	YCplac22	CEN, TRP1
pRK2015	PDC1p-3HA-SUC2-HIS4C	YCplac33	CEN, URA3
pRK2016	PDC1p-VPS68 (TM1)-3HA-SUC2-HIS4C	YCplac33	CEN, URA3
pRK2017	PDC1p-VPS68 (TM1-2)-3HA-SUC2-HIS4C	YCplac33	CEN, URA3
pRK2018	PDC1p-VPS68 (TM1-3)-3HA-SUC2-HIS4C	YCplac33	CEN, URA3
pRK2019	PDC1p-VPS68 (TM1-4)-3HA-SUC2-HIS4C	YCplac33	CEN, URA3

* Gietz and Sugino, 1988